J. Fluid Mech. (1998), *vol.* 362, *pp.* 229–271. Printed in the United Kingdom

Numerical investigation of the turbulent boundary layer over a bump

By XIAOHUA WU AND KYLE D. SQUIRES

Department of Mechanical and Aerospace Engineering, Arizona State University, Box 876106, Tempe, AZ 85287-6106, USA

(Received 12 July 1996 and in revised form 6 January 1998)

Large-eddy simulation (LES) has been used to calculate the flow of a statistically two-dimensional turbulent boundary layer over a bump. Subgrid-scale stresses in the filtered Navier–Stokes equations were closed using the dynamic eddy viscosity model. LES predictions for a range of grid resolutions were compared to the experimental measurements of Webster *et al.* (1996). Predictions of the mean flow and turbulence intensities are in good agreement with measurements. The resolved turbulent shear stress is in reasonable agreement with data, though the peak is over-predicted near the trailing edge of the bump. Analysis of the flow confirms the existence of internal layers over the bump surface upstream of the summit and along the downstream trailing flat plate, and demonstrates that the quasi-step increases in skin friction due to perturbations in pressure gradient and surface curvature selectively enhance near-wall shear production of turbulent stresses and are responsible for the formation of the internal layers. Though the flow experiences a strong adverse pressure gradient along the rear surface, the boundary layer is unique in that intermittent detachment occurring near the wall is not followed by mean-flow separation. Certain turbulence characteristics in this region are similar to those previously reported in instantaneously separating boundary layers. The present investigation also explains the driving mechanism for the surprisingly rapid return to equilibrium over the trailing flat plate found in the measurements of Webster *et al.* (1996), i.e. the simultaneous uninterrupted development of an inner energy-equilibrium region and the monotonic decay of elevated turbulence shear production away from the wall. LES results were also used to examine response of the dynamic eddy viscosity model. While subgrid-scale dissipation decreases/increases as the turbulence is attenuated/enhanced, the ratio of the (averaged) forward to reverse energy transfers predicted by the model is roughly constant over a significant part of the layer. Model predictions of backscatter, calculated as the percentage of points where the model coefficient is negative, show a rapid recovery downstream similar to the mean-flow and turbulence quantities.

1. Introduction

Equilibrium turbulent boundary layers belong to a special class of flows in which mean-flow self-preservation prevails (e.g. see Tennekes & Lumley 1972). In an equilibrium boundary layer production and dissipation of turbulence kinetic energy remain roughly in balance for a significant part of the layer and external conditions that define large-scale structures remain nearly unchanged (e.g. see Townsend 1976). As such, well-defined equilibrium boundary layers have provided a suitable framework for substantially advancing our understanding of turbulent flows using experiments,

theory, and numerical simulation. Most flows encountered in applications, however, are typically subject to perturbations in external conditions, e.g. pressure gradient, curvature, rotation, roughness, blowing and suction, etc. In these flows a well-defined equilibrium condition may no longer exist and boundary layer properties become substantially more complicated. Consequently, current understanding and predictive capabilities of non-equilibrium boundary layers are less well developed than for equilibrium flows.

The particular interest of the present study is large-eddy simulation (LES) of the non-equilibrium turbulent boundary layer flowing over a bump. The bump is formed by a prolonged convex surface with two additional short concave regions fore and aft (figure 1). The flow over the bump permits examination of boundary layer distortion by combined perturbations in streamwise pressure gradient and surface curvature, and recovery following the removal of external perturbations. The particular configuration shown in figure 1 is considered since boundary layer properties have been reported by Webster, Degraaff & Eaton (1996) and provide a means for evaluation of simulation results. As described in §2, the subgrid stress is closed using the dynamic eddy viscosity model of Germano *et al.* (1991). In addition to examination of boundary layer properties, the flow over the bump also affords an appropriate platform for examination of the dynamic model in a strongly distorted non-equilibrium flow.

In §1.1 a survey of previous work on boundary layer response to perturbations in streamwise pressure gradient and surface curvature is presented. An overview of LES and dynamic modelling is summarized in §1.2. In §1.3, the objectives of this study are framed through discussion of three important issues relevant to non-equilibrium turbulent boundary layers.

1.1. *Effects of streamwise pressure gradient and surface curvature*

Boundary layer response to singular perturbations in pressure gradient or curvature, as well as the relaxation of the flow back to an equilibrium condition, has been examined in a number of studies. The individual effect of a step application of curvature on an initially equilibrium turbulent boundary layer is now reasonably well known (e.g. see So & Mellor 1973; Gillis & Johnston 1983; Muck, Hoffmann & Bradshaw 1985; Hoffmann, Muck & Bradshaw 1985; Moser & Moin 1987, Barlow & Johnston 1988). These studies have demonstrated that there is not only a distinction between the effects of concave and convex curvature, but also a substantial distinction between the effects within each category (convex or concave) depending on the strength of the perturbation. Similar to curvature, a step change in streamwise pressure gradient has also been the subject of several investigations (e.g. see Bradshaw & Galea 1967; Samuel & Joubert 1974; Tsuji & Morikawa 1976). Previous work on boundary layer response to pressure gradient has also shown that the flow may exhibit a very different response depending on the strength of the pressure gradient being applied (e.g. separated versus attached). A comprehensive review of separated turbulent boundary layers can be found, for example, in Simpson (1989, and references therein). Spalart & Watmuff (1993) conducted concurrent direct numerical simulations (DNS) and experiments on a flat-plate boundary layer under an adverse pressure gradient. The predicted mean velocity and turbulence intensities were in excellent agreement with the experiments. Recently, Na & Moin (1996) performed a spatially developing DNS on the same flow and reached similar conclusions as those of Spalart & Watmuff (1993).

Investigations of boundary layer response to perturbations in both pressure gradient and curvature show that the combined influence of external perturbations is not a

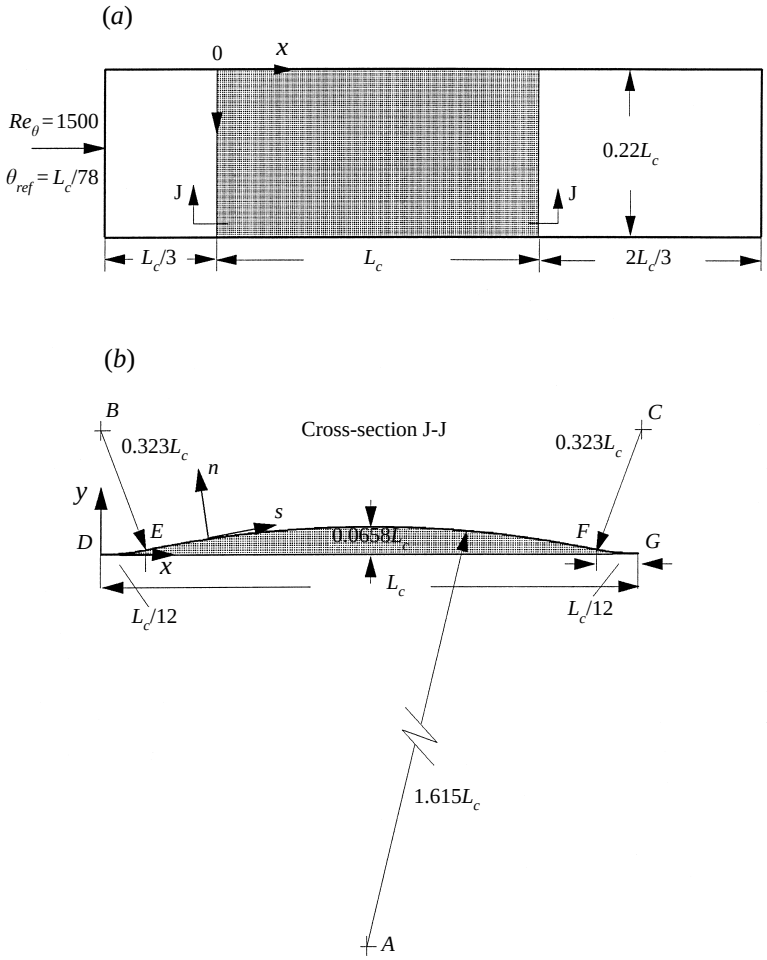

FIGURE 1. (*a*) Top view of the computational domain; (*b*) bump dimensions; D, E, F, G: tangent points; upstream concave surface: $0 \leqslant x_w/L_c \leqslant 1/12$; convex surface: $1/12 \leqslant x_w/L_c \leqslant 11/12$; downstream concave surface: $11/12 \leqslant x_w/L_c \leqslant 1$.

simple summation of their separate effects (e.g. see Smits, Eaton & Bradshaw 1979; Smits & Wood 1985). Relevant to this work are the studies reported by Baskaran, Smits & Joubert (1987), Bandyopadhyay & Ahmed (1993), and Webster *et al.* (1996). Baskaran *et al.* (1987) measured the flow on a hill formed by three tangential arcs (concave, convex, concave). Measurements were made to a location downstream of the summit where separation occurred. 'Knee points' in profiles of the turbulent stresses on the convex surface were attributed to the formation of an internal layer caused by the curvature transition from concave to convex. Baskaran *et al.* (1987) established a threshold criterion in terms of the curvature discontinuity in which an internal layer would form. Properties of the turbulent boundary layer flowing over a bump were measured by Webster *et al.* (1996). In their work the boundary layer did not separate downstream of the summit as in Baskaran *et al.* (1987). Webster *et al.* (1996) attributed most of the response of the boundary layer to streamwise pressure gradient since curvature effects were less apparent in the measurements. They also noted the formation of internal layers related to the step changes in curvature. Signatures of

an internal layer caused by a step change in curvature were also reported in the experimental investigation of Bandyopadhyay & Ahmed (1993).

Parallel to the departure from equilibrium caused by changes in streamwise pressure gradient and surface curvature, the return to equilibrium of a turbulent boundary layer following the removal of these perturbations is also of interest. Bandyopadhyay & Ahmed (1993) found that the skin friction in a boundary layer recovering from a sequence of concave–convex curvature was low and proposed that viscous drag reduction might therefore be accomplished using curvature. Their measurements were similar to the earlier work of Gillis & Johnston (1983) which showed that the recovery of the skin friction is slow in a boundary layer following the removal of prolonged convex curvature (in the absence of external pressure gradients). Gillis & Johnston (1983) also found that turbulence intensities underwent a long recovery and proposed that turbulence structure does not 'spring back' to its original state as if it had been artificially held down by curvature; rather, the eddy structure must slowly enlarge itself in the same way that the turbulence structure of a developing flat-plate boundary layer enlarges itself. In a similar flow Alving, Smits & Watmuff (1990) found that the mean flow approached the unperturbed state monotonically and at a relatively more rapid rate. However, recovery of the turbulent stresses in their experiment was very slow.

The complex response of boundary layers subjected to multiple external perturbations in turn complicates modelling of these non-equilibrium flows. The situation is well described by Bandyopadhyay & Ahmed (1993): 'The modeling is fraught with difficulty because the lag behaviour of large eddies in the simultaneous presence of repeatedly applied complex strains of curvature, pressure gradient, lateral divergence and compressibility, is unknown'. Gibson, Jones & Younis (1981) found, for example, that predictive methods based on modelling the full Reynolds-stress transport equations fail to reproduce the convex-flat relaxation process measured by Gillis & Johnston (1983). Therefore, other approaches are required in order to perform numerical investigations of non-equilibrium boundary layers.

1.2. *LES and dynamic subgrid modelling*

In this work LES of the incompressible Navier–Stokes equations is employed. Since the large eddies are computed directly, only the effect of the smallest (subgrid) scales of motion are modelled. This should be an advantage in simulation of non-equilibrium boundary layers since, although the large eddies may depend significantly on changes in external conditions and flow history, the small eddies probably respond more rapidly to external perturbations. Therefore, it is still reasonable to model the small scales using simple closures, e.g. eddy viscosity formulations such as the dynamic subgrid-scale (SGS) model of Germano *et al.* (1991).

The concept of dynamic modelling is a method for evaluating SGS model coefficients directly from information contained in the resolved turbulent velocity field. The model is formulated to sample turbulent stresses from a band of the smallest resolved scales and then extrapolates this information to the SGS range (e.g. see Meneveau, Lund & Cabot 1996). The implementation involves application of an explicit test filter of width greater than the usual grid filter width, and calculation of the stress tensors in the resolved flow with and without this filter operation. In the eddy viscosity formulation, the assumption that the Smagorinsky model should apply on both scales, and use of an identity, leads to a model coefficient C as a function of position and time, which varies in both magnitude and sign (e.g. see Mason 1994). A negative value of C indicates a flow of energy from the small scales to the resolved

scales, or backscatter, a favourable aspect of the model (Piomelli 1993; Ghosal *et al.* 1995). In practice, the numerical instability associated with locally negative C can be remedied by averaging the coefficient over homogeneous directions which makes it a more smoothly varying function that rarely becomes negative. Ghosal *et al.* (1995) showed that for flows with at least one homogeneous direction the local least-squares minimization introduced by Lilly (1992) for calculation of C coupled with spatial averaging can be derived from a mathematically consistent variational formulation and thus provides a theoretically sound foundation for the model.

Many of the important features of the dynamic eddy viscosity model have been obtained from calculation of equilibrium turbulent flows. Piomelli (1993) applied the model to prediction of turbulent channel flow at a range of Reynolds numbers and presented quantities such as profiles of the model coefficient and its related positive and negative contributions, SGS dissipation (including backscatter), and fraction of points where the coefficient was negative (see also Najjar & Tafti 1996). Piomelli (1993) concluded that one reason the model performs well in wall-bounded flows may be the fact that the eddy viscosity is reduced if subgrid-scale backscatter occurs with significant frequency. Jiménez (1995) analysed the model using simulations of isotropic turbulence and found that the flow rapidly adjusted to artificial perturbations in the model coefficient. The fact that the smallest resolved scales are sampled in the dynamic procedure allows for a relatively rapid change of the coefficient to perturbations in the flow. This feature, together with the fact that the eddy viscosity is sensitive to the smallest resolved scales, allows for adjustments in the subgrid dissipation without an overly adverse effect on the energy in the resolved scales, especially at the lower wavenumbers which are responsible for the majority of momentum and energy transport. It is important to remark that these and other positive aspects of dynamic models, e.g. proper behaviour near walls, are observed in spite of the fact that the model assumes scale similarity at the grid and test levels, conditions seldom satisfied in many LES calculations.

The most important evidence of the robust nature of dynamic models has been demonstrated through their successful application in a wide range of turbulent flows including homogeneous turbulence, channel flow, cavity flow, free shear flows, rotating turbulence, and the backward-facing step (e.g. see Germano *et al.* 1991; Moin *et al.* 1991; Piomelli 1993; Yang & Ferziger 1993; Zang, Street & Koseff 1993; Vreman, Geurts & Kuerten 1994; Piomelli & Liu 1995; Ghosal *et al.* 1995; Lund & Moin 1996; Wu & Squires 1997). In these and other studies LES predictions are as good as or better than other approaches requiring considerably more empirical input.

Previous investigations into the underlying foundation of dynamic models and accurate LES predictions obtained using them motivate their application to complex flows. In this regard, the work of Ghosal *et al.* (1995) on the backward-facing step and Akselvoll & Moin (1995, 1996), who used dynamic models in LES calculations of the flow of co-annular jets discharging into a sudden expansion, are notable examples. In Akselvoll & Moin (1996) the dynamic eddy viscosity model was used to close both the subgrid-scale stresses and subgrid-scale scalar flux. Mean velocity and turbulence intensities were found to be in good agreement with experiments. Since LES provides a time-dependent description of the large scales, Akselvoll & Moin (1996) used simulation results to gain insight into the complex mixing characteristics of the flow.

The reader is referred to Ghosal *et al.* (1995) and Meneveau *et al.* (1996) for further discussion of dynamic models and to Lesieur & Metais (1996) for additional discussion of the applicability of LES for investigating complex turbulent flows.

1.3. *Objectives*

There are several important issues which have arisen from previous examinations of strongly distorted non-equilibrium boundary layers. One of the issues central to this investigation is the generation of internal layers through a discontinuity in surface curvature, as proposed by Baskaran *et al.* (1987). The notion that internal layers are initiated through curvature change is a matter of debate. For example, in a related study by Alving *et al.* (1990), although the criterion established by Baskaran *et al.* (1987) for generation of an internal layer due to curvature change was satisfied in their experiments, signatures of an internal layer could not be found. Alving *et al.* (1990) suggested that the concept of an internal layer growing from the wall with its origin at the curvature discontinuity and remaining uninfluenced by the flow in the parent boundary layer for significant distances, might be too simplistic (see Patel & Sotiropoulos 1997 for further discussion). On the other hand, recent measurements by Webster *et al.* (1996) clearly show distinct 'knees' in profiles of the streamwise intensity downstream of the bump trailing edge and imply the generation of an internal layer. It should also be noted that near the trailing edge the measurements of Webster *et al.* (1996) do not show distinct knee points in the wall-normal and spanwise intensities. Thus, one of the goals of this work is to clarify the existence and provide an improved understanding of the cause of internal layers arising from a discontinuity in curvature.

Subsequent to the initiation of internal layers is their downstream development. Based upon discussion in Baskaran *et al.* (1987) and Webster *et al.* (1996), internal layers generated near the leading edge of the bump are expected to develop continuously downstream to separation or near the trailing edge where another discontinuity in curvature occurs. Because the boundary layer over the surfaces of the bump upstream and downstream of the summit are under streamwise pressure gradients of opposite sign, this would in turn suggest that the adverse pressure gradient downstream of the summit has little effect on the near-wall turbulence, which is inconsistent with measurements from adverse pressure gradient flows (e.g. see Simpson, Chew & Shivaprasad 1981*a*). Therefore, it is also of interest to clarify how the internal layer evolves by studying whether turbulence properties over the rear surface of the bump are a result of the sustained development of a possible upstream internal layer.

In addition to the issues directly linked to the existence, cause, and evolution of internal layers, two important and unusual features emerge from the experiments of Webster *et al.* (1996). They found that, unlike the experiments of Gillis & Johnston (1983) and Alving *et al.* (1990), the boundary layer over the flat plate downstream of the trailing edge exhibits a surprisingly rapid return to equilibrium. The rate of recovery has profound implications on the use of curvature as a means for the control of boundary layer development (e.g. see Bandyopadhyay & Ahmed 1993). Thus, additional insight is needed to explain the driving mechanism behind such an unusually fast return as observed in the experiments. Webster *et al.* (1996) also found that the flow near the trailing edge is on the verge of detachment, though boundary layer separation did not occur. As discussed in Simpson *et al.* (1981*a*), turbulent detachment is a transitory process occurring over a considerable streamwise distance (see also Buckles, Hanratty & Adrian 1984). Thus, it is possible that the boundary layer over the bump may belong to a unique class of flows in that it undergoes possible intermittent detachment, though without mean flow separation. Note in the majority of previous work upstream intermittent transitory detachment results in a downstream separation (see §4.1). Since in LES the time-dependent equations are

solved, it is then possible to examine in detail the near-wall features of the flow in the region of strong adverse pressure gradient, and to compare the statistical properties with existing measurements on instantaneously separating flows.

Therefore, the main objective of this study is to resolve the important issues relevant to boundary layer response to multiple changes in streamwise pressure gradient and surface curvature as described above, i.e. the existence, cause and development of internal layers, the mechanism of return to equilibrium, and the characteristics of a flow on the verge of separation. A numerical investigation is also motivated by the fact that the measurements of the flow over a hill by Baskaran *et al.* (1987) were obtained mostly upstream of the summit due to separation downstream. Experimental measurements in the identical geometry from Webster *et al.* (1996) are limited to the region downstream of the summit. Thus, LES results can be used to provide a complete picture of boundary layer evolution and also facilitate a detailed analysis of the flow.

In addition to the physical insight gained from application of LES to a complex boundary layer, an additional aim of this study is to gain insight into the properties of the dynamic eddy viscosity model in a flow exhibiting strong departure from equilibrium. The response of the model in complex configurations is not easily extrapolated from previous work in canonical flows, e.g. its response as the flow departs from and then returns to equilibrium. The principal focus of this aspect of the study is to examine the behaviour of the model in response to combined perturbations in streamwise pressure gradient and curvature.

The remainder of this paper is organized towards clearly honouring the objectives discussed above. A detailed description of the overall computational approach is first presented in §2, with the governing equations and subgrid-scale model described in §2.1. The numerical method, inflow generation scheme, and other boundary conditions are summarized in §2.2. In order to analyse the simulation results with confidence, it is necessary to establish the accuracy of the LES prior to directly examining flow physics and response of the SGS model. This task is addressed in §3 where predictions of the mean velocity and second-order statistics for a range of grid resolutions, and calculations performed with and without the SGS model, are thoroughly compared with the experimental data of Webster *et al.* (1996). As shown in §3, although some differences between LES predictions and measurements do exist, the calculations reproduce the overall evolution of the boundary layer to a reasonable accuracy and establish the validity of the computational approach for the subsequent analysis of the flow in §4 and response of the model in §5.

2. Simulation overview

2.1. *Governing equations and dynamic SGS model*

The coordinate-independent form of the continuity equation and Navier–Stokes equations for an incompressible fluid are

$$\nabla \cdot \boldsymbol{u} = 0, \tag{2.1}$$

$$\frac{\partial \boldsymbol{u}}{\partial t} + \nabla \cdot (\boldsymbol{u}\boldsymbol{u}) = -\nabla p + \nabla \cdot \left\{ \frac{1}{Re} [\nabla \boldsymbol{u} + (\nabla \boldsymbol{u})^T] \right\}, \tag{2.2}$$

where T denotes the transpose. Solution of the governing equations for the flow over the bump is performed on a set of semi-curvilinear grids. The transformation of the physical domain to a uniform computational space is accomplished by introducing

the mappings

$$\xi = \mathscr{H}_1(x), \qquad \eta = \mathscr{H}_2(x, y), \qquad \zeta = \mathscr{H}_3(z), \tag{2.3}$$

in which the computational grid has a uniform spacing Δ_c. Note that as shown by (2.3), the coordinate planes $\mathscr{H}_1$ = constant and $\mathscr{H}_3$ = constant are Cartesian. An additional restriction imposed is that in physical space the grid spacings along the x- and z-directions are uniform; non-uniform stretching is applied only along the y-direction.

Following Ghosal & Moin (1995), for a fully curvilinear and three-dimensionally non-uniform mapping, the velocity vector $\boldsymbol{u}$ (and similarly for pressure p) is transformed from the physical space to the computational space, $\boldsymbol{u}(x, y, z) \rightarrow \boldsymbol{u}[H(\xi, \eta, \zeta)]$, where H is the inverse of $\mathscr{H}$. The field in computational space is then filtered on the uniform grid

$$\boldsymbol{u}[H(\xi,\eta,\zeta)] \rightarrow \frac{1}{\Delta_c^3}\int\int\int G\left(\frac{\xi-\xi'}{\Delta_c}\right) G\left(\frac{\eta-\eta'}{\Delta_c}\right) G\left(\frac{\zeta-\zeta'}{\Delta_c}\right) \boldsymbol{u}[H(\xi',\eta',\zeta')]\mathrm{d}\xi'\mathrm{d}\eta'\mathrm{d}\zeta'. \tag{2.4}$$

where G is a one-dimensional top-hat filter. Transformation back to physical space yields the filtered field

$$\overline{\boldsymbol{u}}(x,y,z) = \frac{1}{\Delta_c^3}\int\int\int G\left(\frac{\mathscr{H}_1(x)-\xi'}{\Delta_c}\right) G\left(\frac{\mathscr{H}_2(x,y)-\eta'}{\Delta_c}\right) G\left(\frac{\mathscr{H}_3(z)-\zeta'}{\Delta_c}\right) \boldsymbol{u}[H(\xi',\eta',\zeta')]\mathrm{d}\xi'\mathrm{d}\eta'\mathrm{d}\zeta'. \tag{2.5}$$

Application of (2.3)–(2.5) to (2.1) and (2.2) yields the filtered equations governing motion of the large scales

$$\nabla\cdot\overline{\boldsymbol{u}} = 0, \tag{2.6}$$

$$\frac{\partial\overline{\boldsymbol{u}}}{\partial t} + \nabla\cdot(\overline{\boldsymbol{u}}\,\overline{\boldsymbol{u}}) = -\nabla\overline{p} + \nabla\cdot(-\boldsymbol{\tau}) + \nabla\cdot\left\{\frac{1}{Re}[\nabla\overline{\boldsymbol{u}} + (\nabla\overline{\boldsymbol{u}})^T]\right\} + \mathscr{E}_c, \tag{2.7}$$

where $\boldsymbol{\tau}$ is the subgrid-scale stress tensor with Cartesian components τ_{ij}. In (2.6) and (2.7) an overbar denotes the filtered variable, $\overline{\boldsymbol{u}}$ is the resolved velocity vector whose Cartesian components are $(\overline{u},\overline{v},\overline{w})$. Velocities in (2.6) and (2.7) are normalized by the inflow free-stream value U_{ref}, lengths by the bump height h, and $Re = U_{ref}h/\nu$ where ν is the kinematic viscosity. The term $\mathscr{E}_c$ appearing in (2.7) represents the error due to the fact that in general the filtering operation does not commute with differentiation. As demonstrated by Ghosal & Moin (1995), for a fully curvilinear and three-dimensionally non-uniform mapping the commutation error associated with the filtering operation (2.3)–(2.5) is second-order in the filter width, i.e. $\mathscr{E}_c \sim \mathscr{O}(\Delta_c^2)$. Thus, for calculation of spatial derivatives using approximations which are second-order accurate, as in the present work, filtering can be assumed to commute with differentiation, i.e. the error due to lack of commutivity is the same order as the truncation error of the method.

The SGS stress in (2.7), $\tau_{ij} = \overline{u_iu_j} - \overline{u}_i\overline{u}_j$, is parameterized using the Smagorinsky model

$$\tau_{ij} - \frac{\delta_{ij}}{3}\tau_{kk} = -2\nu_T\overline{S}_{ij} = -2C\overline{\Delta}^2|\overline{S}|\overline{S}_{ij}, \tag{2.8}$$

in which δ_{ij} is the Kronecker delta and $|\overline{S}| = (2\overline{S}_{ij}\overline{S}_{ij})^{1/2}$ is the magnitude of the

large-scale strain rate tensor,

$$\overline{S}_{ij} = \frac{1}{2}\left(\frac{\partial \overline{u}_i}{\partial x_j} + \frac{\partial \overline{u}_j}{\partial x_i}\right). \tag{2.9}$$

Note that the trace of the subgrid-scale stress, τ_{kk}, is not modelled; rather it is added to the pressure variable p.

Following Germano *et al.* (1991), a second filter, the test filter (denoted using $\widehat{\ }$) is used to derive an expression for the model coefficient C in (2.8). The key feature of this procedure is use of the identity

$$L_{ij} = T_{ij} - \widehat{\tau_{ij}}, \tag{2.10}$$

which relates the resolved turbulent stress, $L_{ij} = \widehat{\overline{u}_i\overline{u}_j} - \widehat{\overline{u}}_i\widehat{\overline{u}}_j$, the subgrid-scale stress τ_{ij}, and the subtest-scale stress $T_{ij} = \widehat{\overline{u}_i\overline{u}_j} - \widehat{\overline{u}}_i\widehat{\overline{u}}_j$ (Germano 1992). It is assumed that the subtest stresses can be parameterized by an expression similar to that used to model τ_{ij},

$$T_{ij} - \frac{\delta_{ij}}{3}T_{kk} = -2C\widehat{\overline{\Delta}}^2 |\widehat{\overline{S}}|\widehat{\overline{S}}_{ij}. \tag{2.11}$$

On substituting (2.8) and (2.11) into (2.10) a system of five equations for determining C is obtained:

$$L_{ij} - \frac{\delta_{ij}}{3}L_{kk} = -2C\widehat{\overline{\Delta}}^2 |\widehat{\overline{S}}|\widehat{\overline{S}}_{ij} + \widehat{2C\overline{\Delta}^2 |\overline{S}|\overline{S}_{ij}}. \tag{2.12}$$

It is not possible to satisfy (2.12) using a single coefficient C. The error in solving (2.12) should then be minimized (the original formulation in Germano *et al.* 1991 minimized the error by requiring it to be orthogonal to the resolved strain-rate tensor). Ghosal *et al.* (1995) noted that since C appears inside the filtering operation, (2.12) is a system of integral equations. They used a variational approach to minimize the error in a global least-squares sense, leading to a single integral equation for C. Ghosal *et al.* (1995) also showed that simpler expressions for C can be obtained if one places constraints on the coefficient. For example, if C is constrained to have no variation over spatially homogeneous directions and the test filter is applied over these directions, then the following expression is obtained:

$$C = -\frac{1}{2}\frac{\langle L_{ij}M_{ij}\rangle}{\langle M_{ij}M_{ij}\rangle}, \tag{2.13}$$

where

$$M_{ij} = \widehat{\overline{\Delta}}^2 |\widehat{\overline{S}}|\widehat{\overline{S}}_{ij} - \overline{\Delta}^2\widehat{|\overline{S}|\overline{S}_{ij}}. \tag{2.14}$$

In (2.13), $\langle\cdot\rangle$ indicates an average over homogeneous directions, while in (2.14) the filter widths at the subgrid and subtest levels are denoted by $\overline{\Delta}$ and $\widehat{\overline{\Delta}}$, respectively. It should also be noted that (2.13) was obtained by Lilly (1992), in which C was removed from the test filter as in Germano *et al.* (1991) and the error in the resulting system was made orthogonal to M_{ij}. In practice, the 'averaged' coefficient (2.13) is nearly always positive, consistent with the overall transfer of energy being from resolved to subgrid scales.

In the results presented in this paper, averaging of the numerator and denominator in (2.13) is performed over the homogeneous spanwise direction. Note that to be consistent the test filter should then only be applied along the spanwise direction. However, in this study the test filtering operation was performed in physical space

on the coordinate plane $\mathscr{H}_2$ = constant using a top-hat filter of width equal to two mesh spacings. Test filtering on planes $\mathscr{H}_2$ = constant together with (2.13) for determining C is slightly inconsistent since (2.13) requires that the streamwise direction be statistically homogeneous. It is assumed that streamwise variations are relatively small in order to apply (2.13) (see also Ghosal *et al.* 1995; Lund & Moin 1996). Test filtering was performed numerically using Simpson's rule of integration. The coefficient C resulting from the spanwise averaging is time-dependent and a function of the two inhomogeneous coordinates. A clipping function was used to ensure non-negative of values of C following the spanwise averaging applied to (2.13). The effect of this clipping operation is discussed in §5.

2.2. *Numerical method and computational details*

The numerical methodology adopted to solve the filtered continuity and momentum equations (2.6) and (2.7) is the generalized fractional step method (e.g. see Rosenfeld, Kwak & Vinokur 1991; Choi, Moin & Kim 1993). Spatial derivatives are approximated using second-order accurate central differences on a staggered grid. As defined by (2.3), the computational domain is transformed from the Cartesian (x, y, z) system to a body-fitted curvilinear non-orthogonal system (ξ, η, ζ) where ξ is the streamwise coordinate and η is the coordinate normal to the flat plate. The dependent variable $\bar{\mathbf{u}}$ is transformed from $(\overline{u}, \overline{v}, \overline{w})$ to a volume flux vector using area vectors. At the end of each time step, the Cartesian velocity components $(\overline{u}, \overline{v}, \overline{w})$ are recovered to compute the model coefficient C using the procedure given in (2.8)–(2.14). A streamline-normal coordinate system (s, n, z) was used for post-processing with the n-axis perpendicular to the lower surface (figure 1). The corresponding velocity components in the streamline-normal system are denoted $(\overline{u}_s, \overline{u}_n, \overline{u}_z)$. Turbulence statistics were accumulated in both coordinate systems.

Measurements obtained by Webster *et al.* (1996) showed that the bump caused a relatively small distortion of the flow at a location one-third chord length upstream of the onset of curvature ($x/L_c = -1/3$ in figure 1). In order to compare LES predictions to experimental measurements it is necessary to specify in the simulations a realistic, two-dimensional boundary layer at the same location. In the current study, a time-dependent velocity field at the inflow boundary was obtained through a separate LES calculation of a canonical flat-plate boundary layer over a continuous momentum-thickness Reynolds number range $1400 \leqslant Re_\theta \leqslant 1700$. The method used for generating the time-dependent turbulent inflow condition is based on the multiple scale analysis of Spalart (1988), which exploits the slow growth of the flat-plate boundary layer. The main idea is to construct a set of streamwise coordinates along which the application of periodic boundary conditions for the fluctuating turbulent signal (after removing the mean and r.m.s. values) is tolerable (see Spalart 1988). The streamwise length of the domain for the pre-computation is $15\delta_{ref}$. The grid resolution and other dimensions are the same as those in the bump simulation. Further details of the inflow generation are presented in Lund, Wu & Squires (1996, 1998). After a statistically steady state had been achieved, the three velocity components at a streamwise station $Re_\theta = 1500$ were stored for $300\delta_{ref}/U_{ref}$ at a time step $\mathrm{d}t = 0.01\delta_{ref}/U_{ref}$ and were subsequently fed to the inlet ($x/L_c = -1/3$) of the spatially developing bump flow simulation.

The origin of the streamwise (x) coordinate is at the onset of curvature (figure 1). The bump chord-to-height ratio (L_c/h) is 15.2:1. The height of the computational domain is $0.56L_c$ measured from the flat plate ($y = 0$). The length of the upstream and downstream flat plates are $1/3L_c$ and $2/3L_c$, respectively, and the width is $0.22L_c$.

On the top surface of the computational domain, the boundary conditions $\partial\overline{u}/\partial y = 0$, $\overline{v} = 0$, and $\overline{w} = 0$ were applied. At the exit plane a convective boundary condition $\partial\overline{\boldsymbol{u}}/\partial t + V_{conv}\partial\overline{\boldsymbol{u}}/\partial x = 0$ was used (V_{conv} is the bulk velocity at the outlet) together with a correction on the streamwise velocity to ensure global mass conservation (see also Wu & Squires 1995; Akselvoll & Moin 1996). Periodic boundary conditions were applied in the spanwise direction.

The computational grid was generated using the direct distribution control technique of Thomas & Middlecoff (1980), in accordance with the mapping defined in (2.3). The grids were constructed so that the coordinate lines ξ = constant are perpendicular to the flat plate $y = 0$ as well as to the top surface of the computational domain.

Using the inlet profile at $t = 0$ as initial condition, the flow was allowed to evolve for $100\delta_{ref}/U_{ref}$ and statistics were then collected for a period of $200\delta_{ref}/U_{ref}$. Unless otherwise noted $\langle\cdot\rangle$ represents averaging over time as well as along the spanwise direction, the $'$ superscript denotes fluctuating quantities after being subtracted from the mean. 'Upstream' is reserved for streamwise locations upstream of the bump summit (e.g. 'upstream bump surface'), and 'downstream' will be used to indicate locations in the flow downstream of the bump summit. Comparison with the measurements of Webster *et al.* (1996) is made in the Cartesian (x, y, z) system along vertical traverses (constant x); most of the other results are presented in the streamline-normal coordinate system (s, n, z). Finally, the w subscript is reserved for surface values, and the *ref* subscript refers to quantities measured at the inlet station.

3. Simulation validation

A series of calculations was performed to validate the overall computational approach. These simulations are necessary because, although LES is less susceptible to modelling errors than Reynolds-averaged methods, it is still difficult to base subsequent analysis upon results obtained using a single set of numerical parameters. Details of the numerical parameters used in the validation tests are summarized in table 1, where wall units are based on the inflow friction velocity. As shown in the table, the grid resolution used in Case 1, $\Delta x^+ = 44$ and $\Delta z^+ = 21$, is comparable to those in other LES calculations of complex flows (e.g. see Lund & Moin 1996). Filtering was not applied along the wall-normal coordinate due to ambiguities concerning treatment of the mean velocity (e.g. see Horiuti 1993) and the first grid point along the η-coordinate was within one wall unit. Compared to Case 1, the streamwise grid resolution in Case 2 and Case 3 was coarsened by 50%, and the spanwise grid spacing was doubled in Case 3. Results from these cases will be used to demonstrate that the mean and second-order statistics resolved in the LES have converged to an acceptable level with respect to improved grid resolution, bearing in mind that an absolute invariance in LES may not be possible since more turbulence scales are resolved as the grid is refined. In Case 1n and Case 3n, calculations were performed in which no subgrid model was used, which allows assessment of the overall effect of the model through comparison with predictions obtained using the dynamic model at the same grid resolution.

Mean velocity profiles at nine streamwise locations are compared with the experimental measurements of Webster *et al.* (1996) in figure 2. The first station ($x/L_c = -1/3$) is at the inflow boundary and the next eight stations are on the downstream side of the bump. The velocity profiles are normalized by the inflow

Case	(x, y, z)	Δx^+	Δz^+	Model
Case 1	$240 \times 75 \times 65$	44	21	Dynamic
Case 1n	$240 \times 75 \times 65$	44	21	No model
Case 2	$157 \times 75 \times 65$	67	21	Dynamic
Case 3	$157 \times 75 \times 33$	67	42	Dynamic
Case 3n	$157 \times 75 \times 33$	67	42	No model

TABLE 1. Summary of numerical parameters

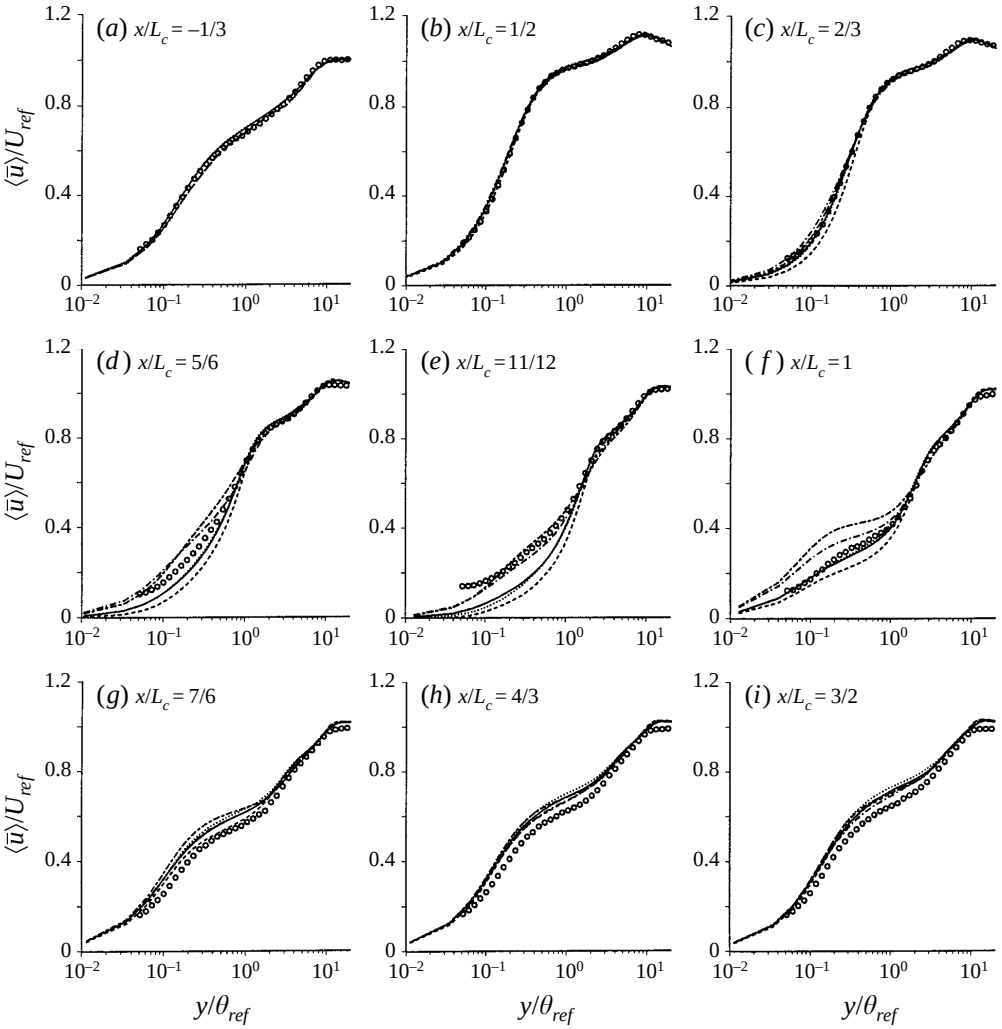

FIGURE 2. Mean velocity $\langle \bar{u} \rangle / U_{ref}$. ○, Webster *et al.* (1996); LES: ——, Case 1; · · · · ·, Case 2; – – – – –, Case 3; — · —, Case 1n; — — —, Case 3n.

free-stream velocity U_{ref}. The vertical coordinate is normalized by the corresponding inflow momentum thickness θ_{ref} based on $99\% U_{ref}$.

At all streamwise stations the predicted mean profiles from Case 1 and Case 2 collapse and are in reasonably good agreement with the experimental measurements of Webster *et al.* (1996). At the inflow boundary the LES pre-computation used

to generate the inflow signal yields a mean profile with a logarithmic region for $30 < y^+ < 200$ (see figure 12*a*). Over the entire downstream side of the bump the agreement between Case 1 and Case 2 LES predictions and experiments is good with the exception of the near-surface region along $x/L_c = 11/12$ (figure 2*e*). At this location the boundary layer exhibits relatively strong intermittent reversal (figure 11). Over the downstream flat plate, LES predictions compare reasonably well with measurements and show a rapid relaxation to the upstream profile. Although not shown here, LES predictions of the mean vertical velocity $\langle\overline{v}\rangle$ are also in good agreement with the experimental data.

With the exception of the three stations near the bump trailing edge, Case 1 and Case 2 results also show small differences from those predicted in Case 3 using the coarsest resolution. At $x/L_c = 5/6$, $11/12$, and 1, Case 3 profiles exhibit a measurable under-prediction compared to those from Case 1 and Case 2 in the near-wall region ($y < \theta_{ref}$). Away from the wall the three sets of results again collapse. Overall, the mean flow for Cases 1–3 is adequately converged with respect to increasing grid resolution. Without the SGS model, the mean velocity predicted in Case 1n and Case 3n is nearly identical with that from Case 1 and Case 3 for $x/L_c < 2/3$ and $x/L_c > 7/6$, indicating that at the given resolution the effect of the model on prediction of the mean flow is small in these regions. Near the trailing edge, no-model predictions of the mean flow exhibit larger differences from the predictions with the model ($x/L_c = 5/6, 11/12$ and 1).

Predictions of the resolved horizontal turbulence intensity are compared with the experimental measurements in figure 3. As shown in figure 3(*a*), the LES pre-computations are in reasonably good agreement with those measured by Webster *et al.* (1996) at the inflow boundary, $x/L_c = -1/3$. At the eight downstream stations the profiles of $\overline{u}'_{rms}/U_{ref}$ from Case 1 and Case 2 have essentially collapsed, and also exhibit small differences compared to the coarser grid Case 3 calculation. Furthermore, the three sets of LES predictions from Cases 1–3 are also in good agreement with the experimental measurements and accurately reproduce several interesting features in the streamwise variations of $\overline{u}'_{rms}$ as found in the experiments. The knee in the profile at the summit (figure 3*b*) is the same as that observed by Baskaran *et al.* (1987) and Webster *et al.* (1996), which results from the destruction of turbulence production in the outer region of the boundary layer by convex curvature and favourable pressure gradient and the development of an internal layer over the upstream convex surface (see §4 for further discussion). The outward shift in the peak streamwise fluctuation near the downstream concave-to-flat tangent (figure 3*d–f*) is typical in turbulent boundary layers experiencing strong adverse pressure gradient (e.g. see Baskaran *et al.* 1987; Simpson 1989). The near-wall peak in the streamwise fluctuations shown in figure 3(*g*) results from the recovery of the inner shear production corresponding to the sudden increase in C_f (cf. figure 10) and the formation of a new internal layer, and the peak away from the wall is a decay of that shown in figure 3(*f*). Note also that the rapid relaxation of the turbulence intensity on the downstream flat plate was also reasonably well captured in the LES calculations. At $x/L_c = 3/2$, the profiles have nearly asymptoted to those at the upstream inlet station. Compared with the LES predictions using the dynamic model, the two sets of no-model calculations, Case 1n and Case 3n, in figure 3 show a noticeable over-prediction of $\overline{u}'_{rms}$, e.g. at $x/L_c = 2/3$ and $11/12$. The deviation of Case 3n predictions from the experimental measurements is substantial, suggesting a relatively large overall effect of the model at the coarsest resolution. At the finer resolution used in Case 1 and Case 1n, the deterioration of the Case 1n predictions is less severe than for Case 3n.

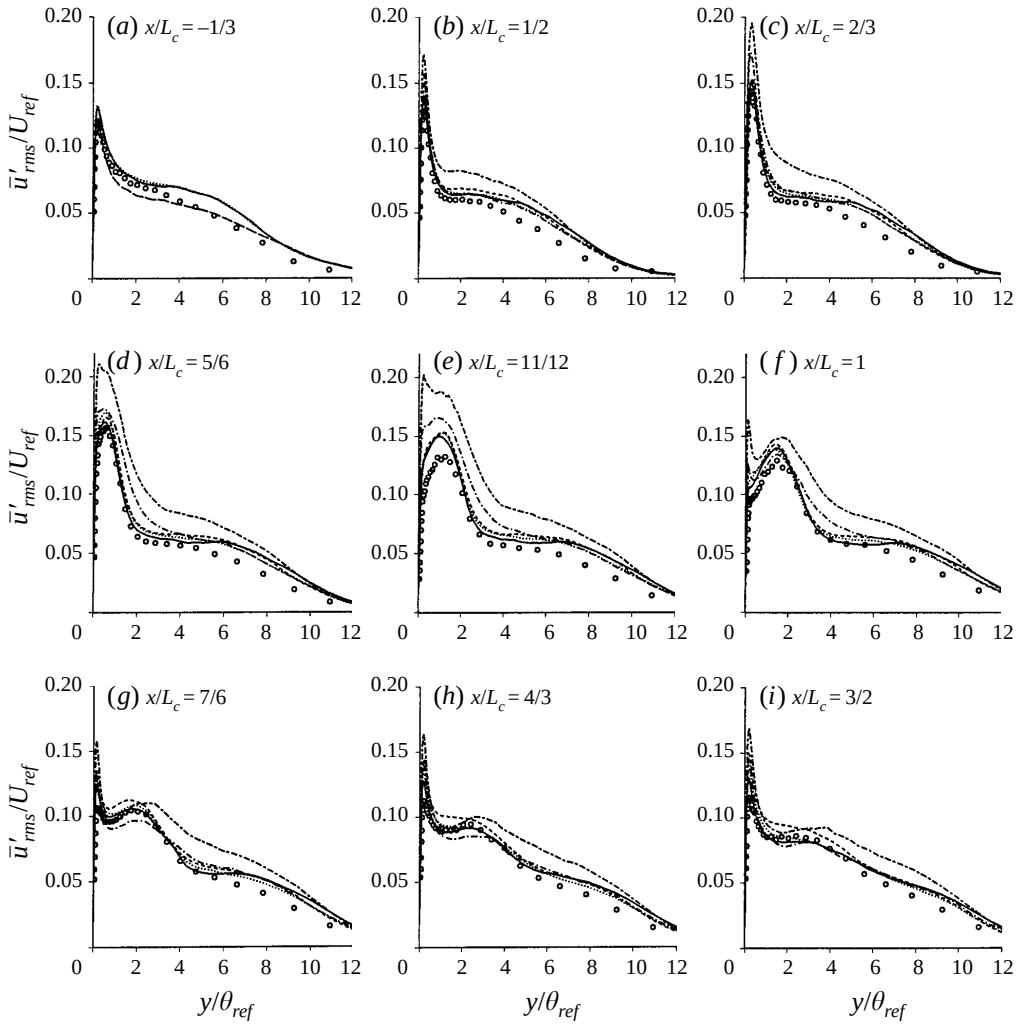

FIGURE 3. Turbulence intensity $\overline{u}'_{rms}/U_{ref}$, for legend refer to figure 2.

Predictions of the vertical and spanwise fluctuating velocities are presented in figure 4 and figure 5, respectively. Similar to the streamwise component, predictions obtained using the dynamic model from Cases 1–3 show relatively small variation with changes in grid resolution. As also clear from figure 4 and figure 5, LES predictions from these cases are in good agreement with the experimental measurements of Webster *et al.* (1996). It is interesting to note that in contrast to the streamwise intensity, $\overline{v}'_{rms}$ and $\overline{w}'_{rms}$ do not exhibit knee points over the summit and downstream of the trailing edge (see §4.1 for further discussion). In calculations without the model (Case 1n and Case 3n), the over-prediction of the vertical and spanwise turbulence intensities is relatively large compared to those obtained using the dynamic model, with the discrepancy more apparent at the coarser resolution used in Case 3n (e.g. see figure 5*c–e*). The spanwise spectra of the turbulence kinetic energy at three representative streamwise stations from the Case 2 and Case 3 calculations are shown in figure 6. Consistent with the mean flow and fluctuations shown in figures 2–5, the spectra show that the flow is reasonably well resolved. Good agreement is

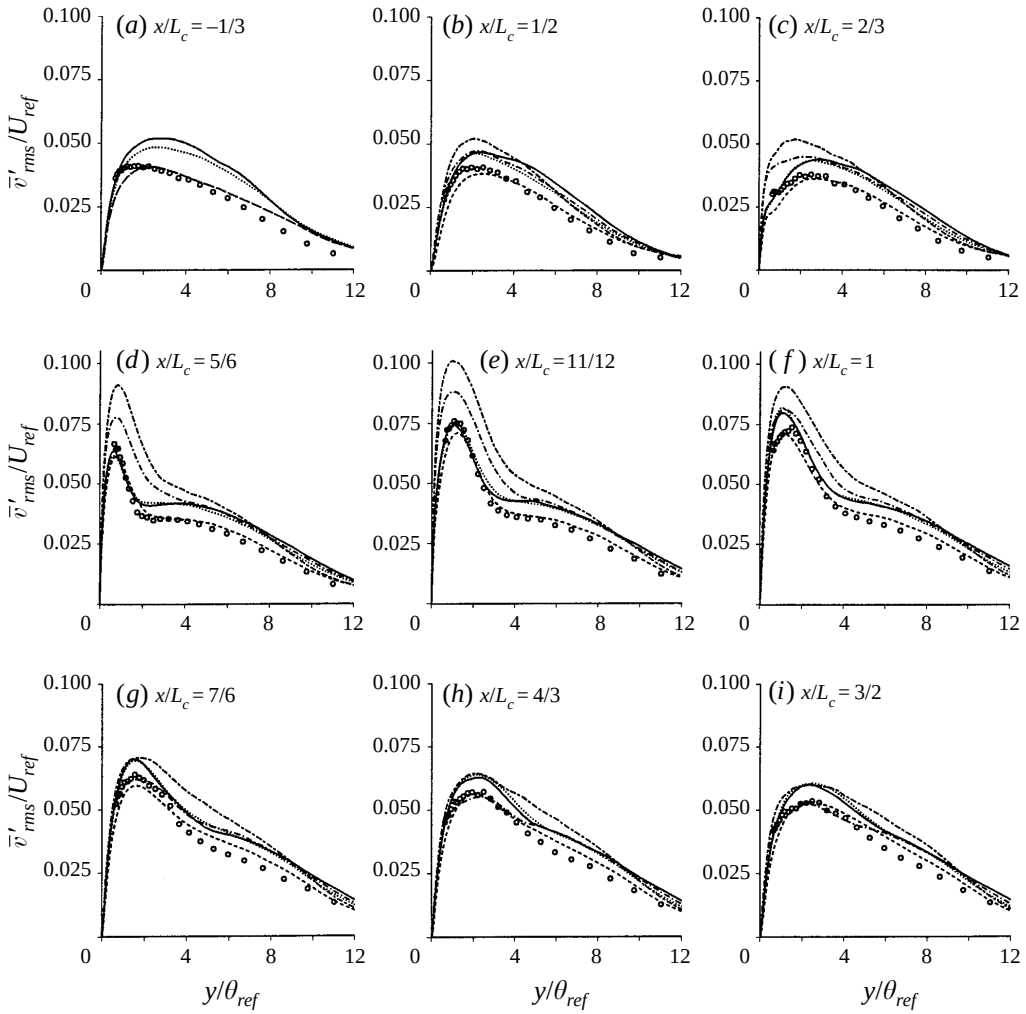

FIGURE 4. Turbulence intensity $\overline{v}'_{rms}/U_{ref}$, for legend refer to figure 2.

also observed between the two calculations, with a slight pile up of energy at high wavenumbers for Case 3. It should also be remarked that, while figure 6 shows that the resolution for Case 2 may be somewhat conservative, it is consistent with requirements in LES with direct application of no-slip boundary conditions, i.e. relatively fine grid spacings are required to resolve near-wall structures. While the drawback is that LES calculations are Reynolds number dependent, less burden is placed on the subgrid model, thus reducing errors introduced through the use of (2.8).

Predictions of the resolved turbulent shear stress $-\langle\overline{u}'\overline{v}'\rangle$ are shown in figure 7. Figure 7(*a*) shows that the shear stress from the LES pre-computation used to generate the inflow condition is higher than that measured by Webster *et al.* (1996) for Case 1 and in good agreement with the experiments for Case 3. At the summit, $x/L_c = 1/2$, LES predictions of the reduction in the shear stress by convex curvature and favourable pressure gradient are in reasonably good agreement with measurements, with a slight over-prediction as evident in the figure. For the streamwise positions along the rear bump surface shown in figure 7(*c–f*) where the boundary layer

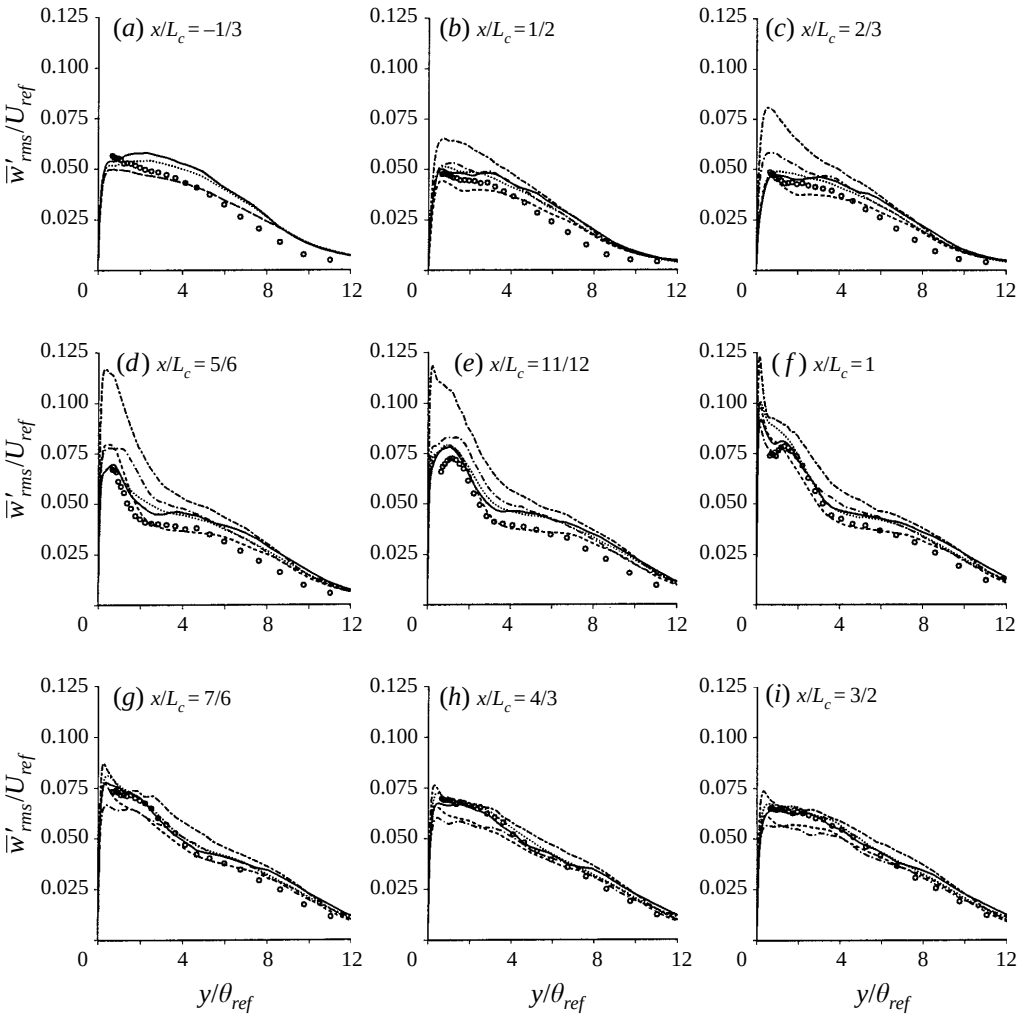

FIGURE 5. Turbulence intensity $\overline{w}'_{rms}/U_{ref}$, for legend refer to figure 2.

experiences strong adverse pressure gradient, LES predictions capture the significant increase in the shear stress near the wall. In this region, figure 7(*b–f*) also shows that LES predictions performed with the dynamic model from Cases 1–3 are essentially insensitive to changes in resolution. In the recovery region over the downstream flat plate, shear stress profiles from Cases 1–3 exhibit slightly larger differences, with an over-prediction in peak levels apparent at $x/L_c = 1$ and $7/6$. The convergence in the shear stress for Cases 1–3 is similar to that observed in the turbulence intensities shown in figures 3–5 and shows that the fluctuations have been reasonably well resolved. Figure 7(*c–e*) also shows that the shear stress is over-predicted in Case 1n and Case 3n where no subgrid model was used. The over-prediction (especially in the outer region) persists downstream of the trailing edge for the coarser resolution used in Case 3n. However, for the finer resolution no-model calculation (Case 1n), the peak shear stress in the recovery region is in better agreement with measurements than in Case 1. It should be noted that the peak in the shear stress profile over the downstream flat plate is a result of the decay of those shown in figure 7*d*, *e*, which

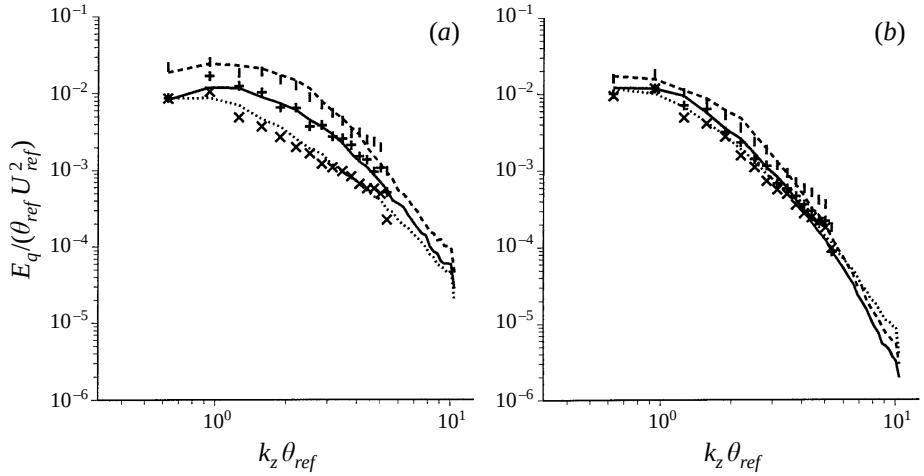

FIGURE 6. Spanwise spectra of turbulence kinetic energy, lines Case 2; symbols: Case 3. ——, +, $x/L_c = 0$; · · · · ·, ×, 1/2; – – – – –, |, 1. (*a*) $y/\theta_{ref} = 1$; (*b*) $y/\theta_{ref} = 3$.

are produced under strong adverse pressure gradient. Apparently, at finer resolution the no-model calculation yields a more rapid rate of decay than obtained using the dynamic model.

Overall, there is good agreement between LES predictions of the mean flow and second-order statistics from Cases 1–3 and the experimental data of Webster *et al.* (1996). The mean flow and fluctuating velocities are accurate and in good agreement with measurements. The largest discrepancy between predictions and measurements occurs in the shear stress. LES predictions of the enhancement and recovery of the shear stress, for example, are relatively accurate except for a few locations near the wall. As demonstrated in figures 2–7, the flow is reasonably well resolved and relatively insensitive to changes in grid resolution. Therefore, the effect of numerical errors (e.g. discretization error, etc.) on prediction of the shear stress is relatively small. One complicating feature of the flow is that the boundary layer on the rear surface of the bump is on the verge of separation, experiencing intermittent reversal in the region of over-predicted shear stress (cf. figure 8, figure 11). Previous measurements on adverse pressure gradient flows have shown that intermittent detachment results in large shear stress just outside the region of instantaneous backflow. Differences between computation and experiment leading to relatively stronger effects of intermittent backflow in the LES would in turn yield larger shear stress.

Some of the differences between LES and experiment are caused by errors in the subgrid model. The SGS model used in this work is based on an eddy viscosity formulation which requires that the principal axes of the SGS stress tensor be aligned with the resolved strain rate. In addition, the expression for the eddy viscosity is based on equilibrium between production and dissipation of turbulence kinetic energy. Alignment between stress and strain is restrictive and in regions of the flow where there are strong departures from equilibrium (e.g. near the trailing edge of the bump), eddy viscosity models should not be expected to be as accurate. Mixed models in which the SGS stress and resolved strain rate are not aligned would presumably yield a more accurate accounting of non-equilibrium effects (e.g. Zang *et al.* 1993). Nevertheless, previous work has shown that even eddy viscosity models tend to adjust to yield approximately the correct level of SGS dissipation (e.g. see Akselvoll &

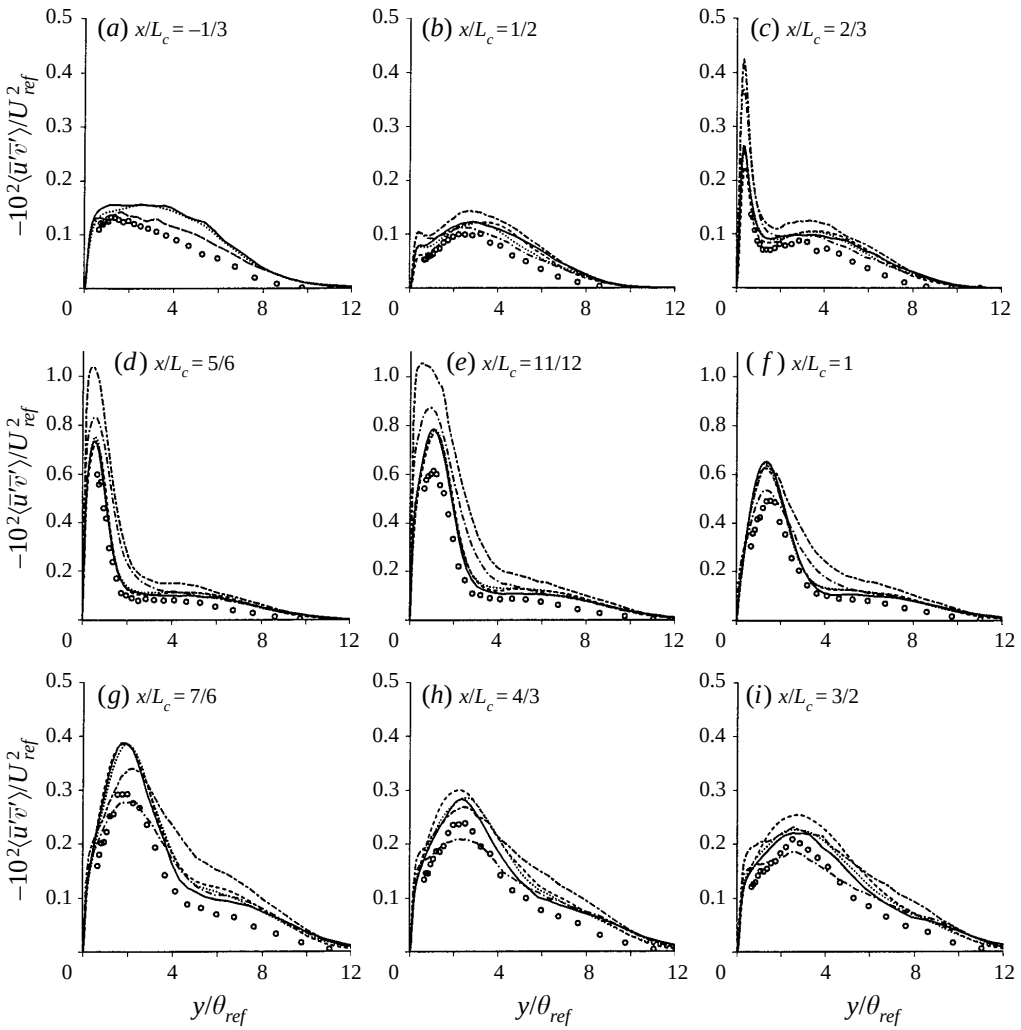

FIGURE 7. Resolved turbulent shear stress $-\langle \overline{u}'\overline{v}' \rangle / U_{ref}^2$, for legend refer to figure 2.

Moin 1995). In the present calculations, without the contribution of the SGS model (Case 1n and Case 3n), fluctuation levels are over-predicted, showing the positive role played by the dynamic model.

In summary, the results presented in this section demonstrate that the strong departure from, and return to, equilibrium in the mean flow and turbulence intensities have been captured in the LES, both qualitatively and quantitatively. As the flow passes over the bump, the turbulent shear stress experiences large streamwise variations, i.e. substantial suppression over the summit by favourable pressure gradient and convex curvature, strong elevation near the trailing edge due to adverse pressure gradient and concave curvature, and a rapid relaxation over the downstream flat plate as the perturbations are removed. These features have all been reasonably well captured in the LES. As discussed above, peak values of the shear stress are over-predicted. However, we believe this discrepancy between measurements and simulations does not invalidate use of the calculations to analyse the flow and examine response of

the model. Unless otherwise stated, the results to be presented in §4 and §5 are from Case 1.

4. Flow analysis

4.1. *Overall boundary layer development*

The surface static pressure coefficient, $C_{pw} = (\langle \overline{p}_w \rangle - \langle \overline{p}_{w,ref} \rangle)/\frac{1}{2}U_{ref}^2$, is compared with the experimental measurements of Webster *et al.* (1996) in figure 8(*a*). There is good agreement between the simulation results and experimental measurements. The figure shows that the streamwise pressure gradient is mildly adverse over the upstream flat plate. Near the bump, C_{pw} increases rapidly, i.e. the streamwise pressure gradient becomes strongly adverse. Over the upstream concave surface, this relatively strong adverse pressure gradient changes to significantly favourable within a short distance. From the middle of the upstream concave surface to the bump summit, C_{pw} decreases monotonically to its minimum value, i.e. the pressure gradient is decreasingly favourable. Downstream of the summit the streamwise pressure gradient is strongly adverse and changes to mildly favourable over the flat plate. Figure 8(*b*) shows the distributions of the non-dimensional pressure gradient parameters,

$$P_g = \frac{\mathrm{d}\langle \overline{p}_w \rangle}{\mathrm{d}s}\frac{\theta_{ref}}{U_{ref}^2}, \qquad P^+ = \frac{\nu}{\sigma_w^{1.5}}\frac{\mathrm{d}\langle \overline{p}_w \rangle}{\mathrm{d}s}, \tag{4.1}$$

where σ_w is the wall shear stress. The three streamwise locations where P_g and P^+ change sign (adverse-to-favourable, favourable-to-adverse, and adverse-to-favourable) are $x_w/L_c = 0.05$, 0.5, and 1.0, respectively. The two transitions from adverse to favourable occurring in the concave surfaces are sudden and may be classified as step changes. The transition from favourable to adverse at the bump summit is gradual. Also shown in figure 8(*b*) are the threshold values suggested by Patel (1965) for onset of the processes of separation ($P^+ = 0.09$) and relaminarization ($P^+ = -0.018$). For $0.67 < x_w/L_c < 0.99$, $P^+ > 0.09$, and in this region the boundary layer experiences intermittent reversal in a thin region near the wall but on average remains attached (see figure 11).

Figure 9(*a*) shows the integral parameters. Unless otherwise stated, the boundary layer thickness δ_s, displacement thickness δ_s^* and momentum thickness θ_s are calculated in the (n, s) system based on 99% of the local edge velocity $U_e(n, s)$. The variations of θ_s, δ_s^* and δ_s^*/θ_s (the shape factor) are qualitatively similar to those measured in the flow over a hill by Baskaran *et al.* (1987). The constant shape factor on the downstream flat plate indicates that the flow is relaxing towards equilibrium (see also Bandyopadhyay & Ahmed 1993). This relaxation process is more clearly shown in figure 9(*b*) where the Clauser parameter G is plotted against the streamwise pressure gradient parameter β following Bandyopadhyay & Ahmed (1993),

$$G = \frac{\displaystyle\int_0^{\delta_s} [(U_e - \langle \overline{u}_s \rangle)/U_\sigma]^2 \mathrm{d}n}{\displaystyle\int_0^{\delta_s} [(U_e - \langle \overline{u}_s \rangle)/U_\sigma] \mathrm{d}n}, \qquad \beta = \frac{\delta_s^*}{\sigma_w}\frac{\mathrm{d}\langle \overline{p}_w \rangle}{\mathrm{d}s}, \tag{4.2}$$

where U_σ is the friction velocity. At the inlet, the LES pre-computation yields the equilibrium value $G \approx 6$ (e.g. see Tennekes & Lumley 1972). Over the upstream flat plate the departure from equilibrium ($G \approx 6, \beta = 0$) is along positive β (adverse pressure gradient) with an increase in G. At the onset of curvature, G turns back

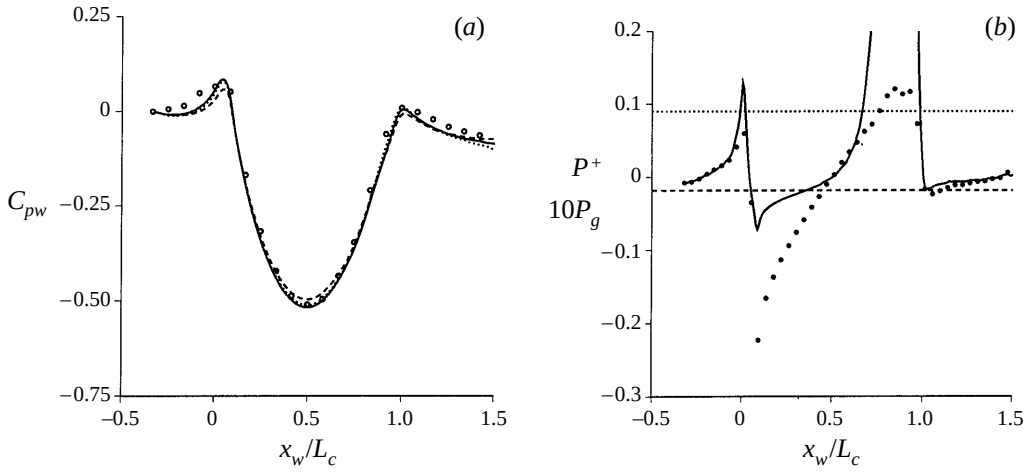

FIGURE 8. Wall-static pressure coefficient and non-dimensional pressure gradient parameter. (*a*) C_{pw}: ○, Webster *et al.* (1996); LES: ——, Case 1; · · · · ·, Case 2; – – – – –, Case 3; (*b*) •, $10P_g$; ——, P^+; · · · · ·, P^+ separation threshold from Patel (1965); – – – – –, P^+ relaminarization threshold from Patel (1965).

with the reduction of adverse pressure gradient; β changes sign in the middle of the concave surface (see also figure 8*b*). The second turning point in the trajectory occurs at the (upstream) concave-to-convex tangent where the pressure gradient starts to become less favourable. In the region of decreasing favourable pressure gradient upstream of the summit the Clauser parameter exhibits relatively little change, but the strong adverse pressure gradient on the downstream side carries the flow to a strong departure from equilibrium (note that the trajectory is closed but cannot be shown completely on the present scale due to this strong departure). Over the downstream concave surface, β sharply decreases (decreasing adverse pressure gradient) and on the downstream flat plate G relaxes back towards its inlet value. At $x/L_c = 3/2$, $G = 5.7$, within 6% of the upstream equilibrium value.

The skin friction coefficient, $C_f = \sigma_w/\frac{1}{2}U_{ref}^2$, is shown in figure 10(*a*). The friction coefficient exhibits an interesting response to the combined perturbations in pressure gradient and curvature. Generally speaking, C_f tends to decrease when a boundary layer is subjected to adverse pressure gradient or convex curvature; favourable pressure gradient or concave curvature tends to increase C_f (e.g. see Bandyopadhyay & Ahmed 1993). The distribution shown in figure 10(*a*) is similar to that measured by Baskaran *et al.* (1987) over a hill. The decrease in C_f for $0.15 < x_w/L_c < 0.5$ is due to the the dominance of convex curvature over favourable pressure gradient; the plateau for $0.75 < x_w/L_c < 0.85$ is related to the incipient detachment occurring in this region (see figure 11). Near the leading and trailing edge of the bump C_f exhibits rapid increases at locations where the streamwise pressure gradient undergoes step changes from adverse to favourable. The rapid increases in C_f and step changes in pressure gradient also occur near curvature transitions (flat-to-concave upstream of the summit and convex-to-concave downstream of the summit).

The two abrupt increases in C_f imply quasi-step changes in the near-wall velocity gradient $\partial\langle\overline{u}_s\rangle/\partial n$. Thus, production terms dependent on $\partial\langle\overline{u}_s\rangle/\partial n$ in the transport equations for second-order turbulence statistics will be expected to show large increases in the near-wall region. In particular, shear production of the streamwise intensity, Reynolds shear stress, and turbulence kinetic energy in the boundary

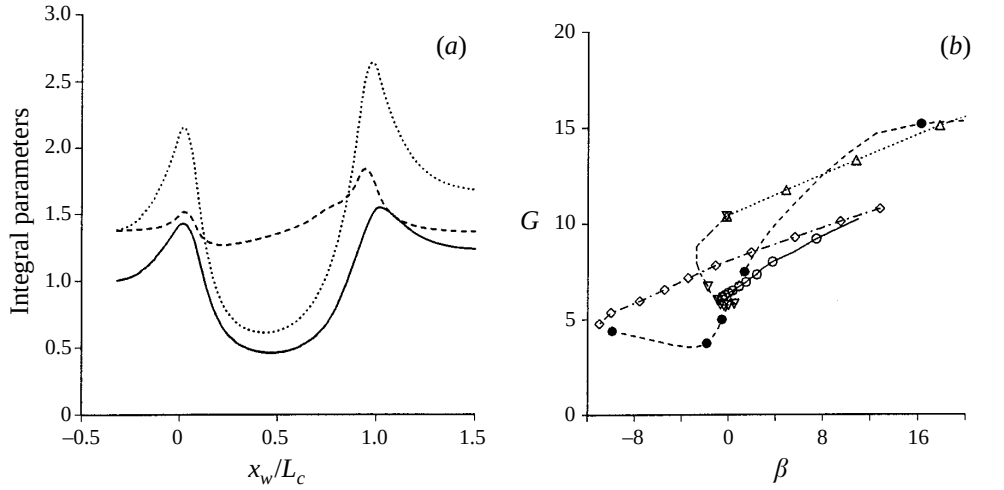

FIGURE 9. Variation of integral parameters. (*a*) ——, θ_s/θ_{ref}; · · · · ·, δ_s^*/θ_{ref}; – – – – –, δ_s^*/θ_s; (*b*) trajectory of Clauser parameter G as a function of β: ○, upstream flat plate, ◇, upstream concave surface; ●, convex surface; △, downstream concave surface; ∇, downstream flat plate.

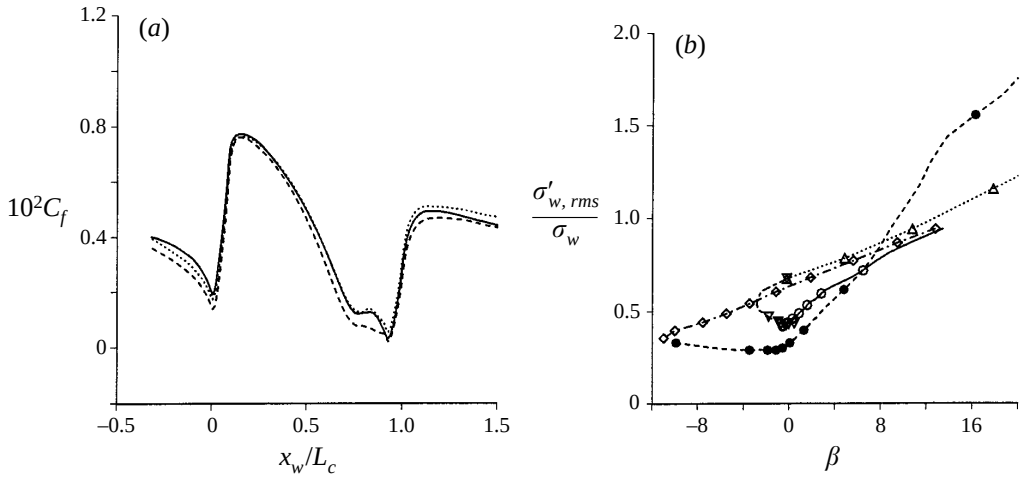

FIGURE 10. Variation of skin friction coefficient and r.m.s. streamwise wall-shear stress fluctuation. (*a*) C_f: ——, Case 1; · · · · ·, Case 2; – – – – –, Case 3; (*b*) trajectory of $\sigma'_{w,rms}/\sigma_w$ as a function of β: ○, upstream flat plate; ◇, upstream concave surface; ●, convex surface; △, downstream concave surface; ∇, downstream flat plate.

layer Reynolds stress transport equations over curved surfaces involve $\partial\langle\overline{u}_s\rangle/\partial n$, and can be expressed as $-\langle\overline{u}'_s\overline{u}'_n\rangle(1 + n/R)\partial\langle\overline{u}_s\rangle/\partial n$, $\langle\overline{u}'^2_n\rangle(1 + n/R)\partial\langle\overline{u}_s\rangle/\partial n$, and $-\langle\overline{u}'_s\overline{u}'_n\rangle(1 + n/R)\partial\langle\overline{u}_s\rangle/\partial n$, respectively (Gibson *et al.* 1981). On the other hand, shear production terms of the wall-normal and spanwise intensities do not directly involve $\partial\langle\overline{u}_s\rangle/\partial n$. Thus, if the quasi-step change in C_f is central to the explanation of internal layer generation at a curvature discontinuity, signatures (knee points, for example) should manifest themselves first in the distributions of the streamwise intensity, kinetic energy, and shear stress rather than wall-normal and spanwise intensities. It should be noted that this is in fact the case in the measurements of Webster *et al.* (1996) (see figures 3–5). The present proposition that a quasi-step increase in C_f selectively

modifies near-wall shear production of turbulent stresses and leads to formation of an internal layer will be further elaborated in §4.2.

The variations of the relative intensity of streamwise fluctuating wall shear stress $\sigma'_{w,rms}/\sigma_w$ with β are shown in figure 10(*b*). Along the upstream flat plate, the two concave surfaces and the downstream convex surface $\sigma'_{w,rms}/\sigma_w$ vary almost linearly with β. It is also clear that over the upstream convex surface ($\beta < 0$) $\sigma'_{w,rms}/\sigma_w$ is relatively constant and therefore nearly unaffected by the decreasing favourable pressure gradient and the suppressing effect of convex curvature. This in turn shows that the nature of the near-wall turbulence over the upstream convex surface is different from that over most of the downstream bump surface. As discussed in §4.3 using the budget equation of the turbulence kinetic energy, there exists an inner energy-equilibrium region on the upstream convex surface. The distinctly different distributions of $\sigma'_{w,rms}/\sigma_w$ before and shortly downstream of the summit is one of the indications that development of the inner region is interrupted by the strong adverse pressure gradient along the downstream surface. Along the downstream flat plate, the relative r.m.s. wall shear stress fluctuations return rapidly to the upstream equilibrium levels. At $x/L_c = 3/2$, $\sigma'_{w,rms}/\sigma_w$ is within 6% of the inlet value.

In a boundary layer subjected to adverse pressure gradient, the near-wall flow may exhibit intermittent reversal. The degree of intermittent reversal can be quantified using a surface forward-flow intermittency factor, $\gamma_{+,w}$, which is defined as the fraction of time that the surface streamline is in the downstream direction, i.e. $\sum t(\overline{u}_{s,w} > 0)/\sum t$ (Simpson *et al.* 1981*a*). Incipient detachment is defined as instantaneous backflow 1% of the time ($\gamma_{+,w} = 0.99$); intermittent transitory detachment occurs with instantaneous backflow 20% of the time ($\gamma_{+,w} = 0.80$); transitory detachment is defined as instantaneous backflow 50% of the time ($\gamma_{+,w} = 0.50$). Figure 11(*a*) shows that the surface streamline along the downstream side of the convex surface experiences incipient detachment at $x_w/L_c = 0.7$ and intermittent transitory detachment at $x_w/L_c = 0.86$, but does not undergo transitory detachment, in qualitative agreement with the visualizations discussed in Webster *et al.* (1996). Figure 11(*a*) also shows that $\gamma_{+,w}$ develops slowly upstream of the maximum backflow station ($\gamma_{+,w} = 0.56$ at $x/L_c = 0.92$), but relaxes quickly back to unity downstream; similar behaviour was observed by Na & Moin (1996) in a separated flat-plate boundary layer. After the maximum backflow station, the second downstream location where $\gamma_{+,w} = 0.80$ is attained at $x_w/L_c = 0.96$ and $\gamma_{+,w} = 0.99$ at $x_w/L_c = 1.02$. Such asymmetry can be more clearly seen in figure 11(*b*) where the wall-normal profiles of the backflow intermittency factor $\gamma_-(n) = \sum t\{\overline{u}_s(n) < 0\}/\sum t$ are shown. The extent of the intermittent backflow region is limited to a thin layer close to the surface with a maximum wall-normal extent $0.95\theta_{ref}$. It is interesting that the results shown in figure 11 indicate that the present boundary layer over the rear surface within $0.7 \leqslant x_w/L_c \leqslant 1.02$ belongs to a unique category in that the upstream intermittent detachment occurring between $x_w/L_c = 0.7$ and 0.92 does not lead to a downstream mean flow separation. Rather, the downstream layer undergoes an intermittent reattachment between $x_w/L_c = 0.92$ and 1.02. In previous studies, instantaneously detaching flows are followed by a downstream mean flow separation and instantaneously reattaching flows are proceeded by a detachment (e.g. see Simpson *et al.* 1981*a*, *b*; Buckles *et al.* 1984 and Singh & Azad 1995*a*, *b*). Thus, it is of interest to compare the behaviour of turbulence statistics in these two types of flows.

Wall-normal profiles of the mean streamwise velocity are shown in figure 12. Generally, favourable pressure gradient and concave curvature tend to reduce the

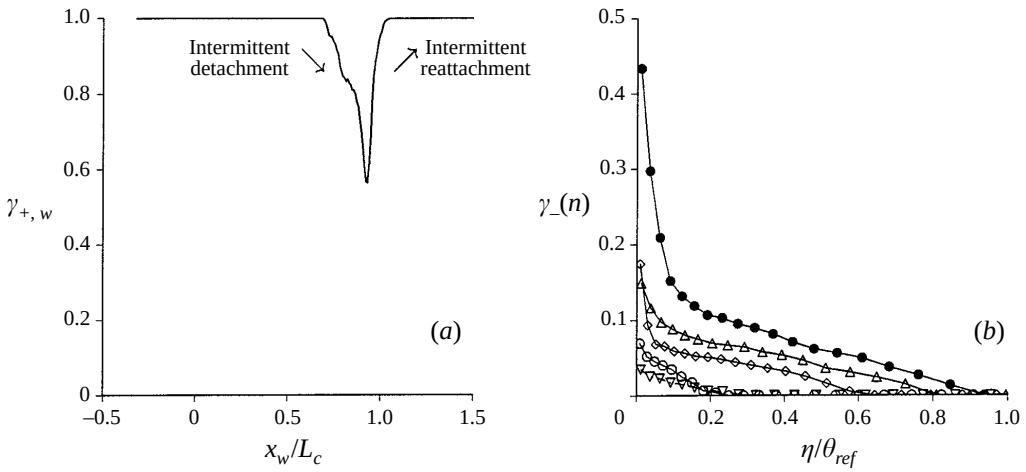

FIGURE 11. Variation of intermittency factors. (*a*) $\gamma_{+,w}$; (*b*) $\gamma_{-}(n)$: ○, $x_w/L_c = 3/4$; ◇, 5/6; ●, 11/12; △, 23/24; ▽, 1.

wake factor, adverse pressure gradient and convex curvature tend to increase it (e.g. see Moser & Moin 1987). Figure 12(*a*) shows that the mild adverse pressure gradient over most of the upstream flat plate does not cause a significant distortion of the profiles. As the flow approaches the bump, the relatively strong adverse pressure gradient near the flat-to-concave tangent causes $\langle \overline{u}_s \rangle^+$ to rise noticeably above the log law, the upstream concave surface and strong favourable pressure gradient then cause the mean profile to dip below the logarithmic region at $x_w/L_c = 1/24$. Similar behaviour was observed in the experiments of Baskaran *et al.* (1987) and Barlow & Johnston (1988). Over the upstream convex surface (figure 12*b*), the profiles collapse well below $n^+ = 10$, but not further away from the wall. Figure 12(*c*) shows that over the downstream side of the bump in the region of strong adverse pressure gradient the profiles are strongly distorted compared to the log law. Unlike the flow over the upstream convex surface, the profiles do not collapse even below $n^+ = 10$ and the degree of departure from equilibrium is very strong in this region. Figure 12(*c*) also shows that at $x_w/L_c = 23/24$, concave curvature again causes the profile to dip compared to the profile at $x_w/L_c = 11/12$. Perry & Schofield (1973) found that the mean velocity profiles in many adverse pressure gradient boundary layers with $-\langle \overline{u}_s' \overline{u}_n' \rangle_{max} > 1.5\sigma_w$ (as in the present flow) obey a half-power law. Although not shown here, the velocity profiles on the downstream convex surface do not obey the Perry–Schofield half-power law, which further highlights the significant departure from equilibrium of the boundary layer. On the downstream flat plate, the profiles at $x_w/L_c = 7/6$, 4/3 and 3/2 collapse below $n^+ = 10$, similar to those shown in figure 12(*b*). Following the removal of the pressure gradient and curvature perturbations, the mean flow relaxes back towards its inlet profile. At $x_w/L_c = 3/2$ (less than four reference boundary layer thicknesses from the removal of curvature), $\langle \overline{u}_s \rangle^+$ has a logarithmic region to about $n^+ = 80$. Measurements from Webster *et al.* (1996) show that by six reference boundary layer thicknesses following the removal of curvature the mean velocity has fully recovered to the flat-plate profile. Thus, both the simulations and experiments show a rapid return to equilibrium of the mean flow.

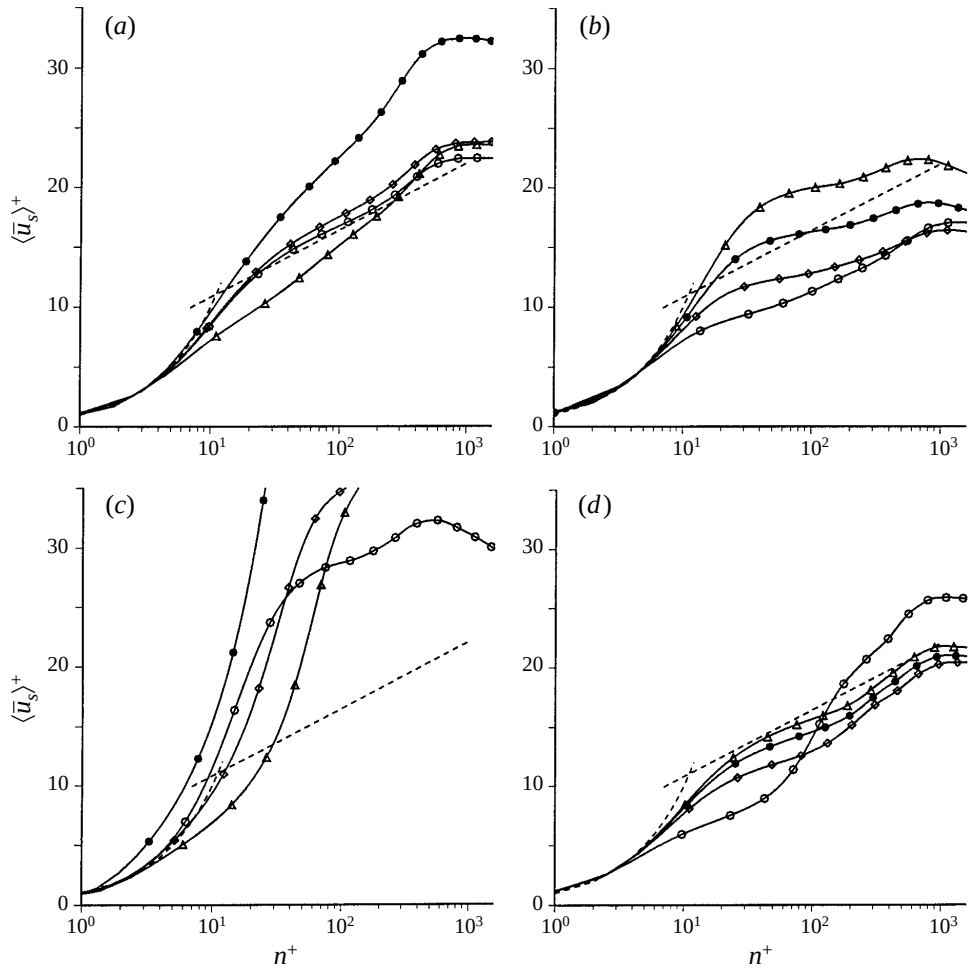

FIGURE 12. Mean streamwise velocity in wall coordinates: (*a*) upstream flat plate and concave surface: ○, $x_w/L_c = -3/10$; ◇, $-1/6$; ●, 0; △, 1/24; (*b*) upstream convex surface: ○, 1/12; ◇, 1/6; ●, 1/3; △, 1/2; (*c*) downstream convex and concave surfaces: ○, 2/3; ◇, 5/6; ●, 11/12; △, 23/24; (*d*) downstream flat plate: ○, 1; ◇, 7/6; ●, 4/3; △, 3/2; – – – –, $\langle \overline{u}_s \rangle^+ = n^+$, $\langle \overline{u}_s \rangle^+ = 2.44 \ln(n^+) + 5.2$.

4.2. *Turbulence statistics*

Wall-normal profiles of the turbulence kinetic energy K are shown in figure 13 to further elucidate the first two issues outlined in §1.3, i.e. existence and development of the internal layers, and the process of return to equilibrium. As shown in figure 13(*a*), the weak adverse pressure gradient on the upstream flat plate has a small effect on the kinetic energy. Close to the wall the adverse pressure gradient causes K to slightly increase, and this increase continues as the flow approaches the bump. At the onset of curvature ($x_w/L_c = 0$), the relatively large adverse pressure gradient has caused a 30% increase in the peak K compared to the inlet value. Comparison of the profile at the onset of curvature to that in the middle of the concave surface ($x_w/L_c = 1/24$) immediately after the adverse-to-favourable pressure gradient transition indicates that beyond $n/\theta_{ref} = 0.5$, K is unchanged and therefore has not been affected by either the adverse-to-favourable pressure gradient transition or the concave surface. Close

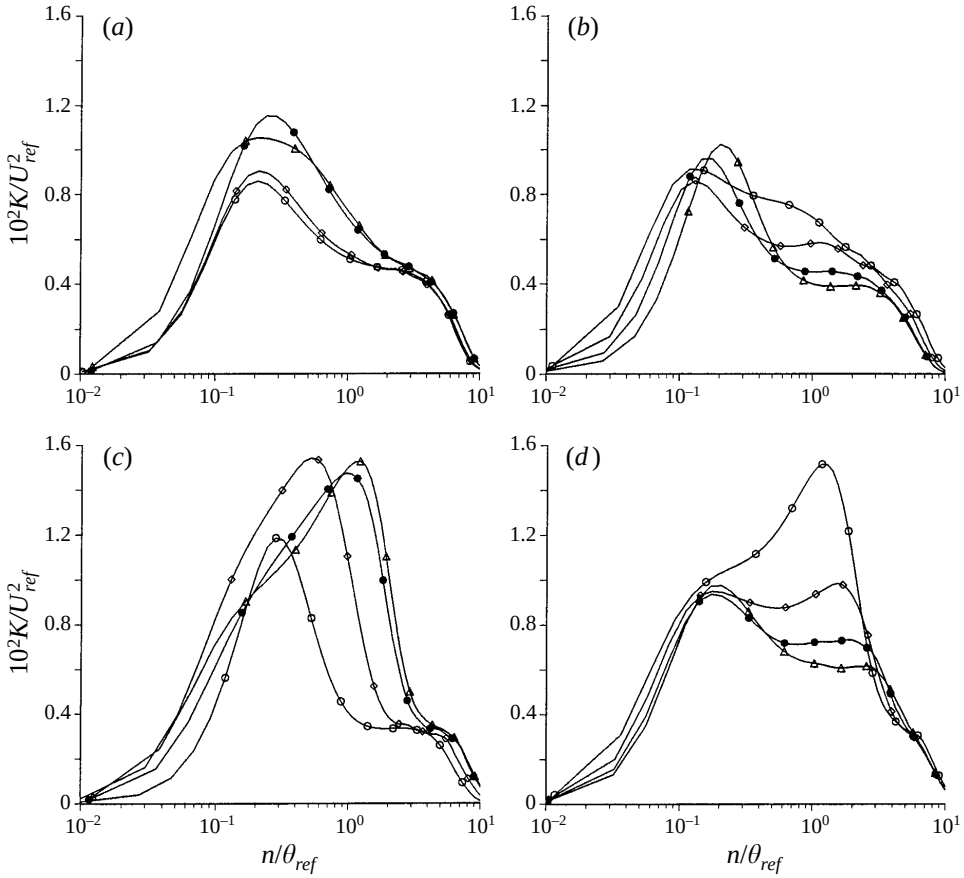

FIGURE 13. Turbulence kinetic energy, for legend refer to figure 12.

to the wall the kinetic energy is influenced by the favourable pressure gradient as evidenced by the decrease in the peak value.

Figure 13(*b*) shows that at the exit of the upstream concave surface ($x_w/L_c = 1/12$), the peak kinetic energy has decreased by 20% compared to the value at $x_w/L_c = 0$. Over the upstream convex surface ($x_w/L_c = 1/6, 1/3, 1/2$), several interesting features in the profiles are apparent. For a large part of the layer ($0.6 < n/\theta_{ref} < 4$) K decreases downstream under the stabilizing effect of favourable pressure gradient and convex curvature; however, the peak in the profile increases with downstream evolution. This increase takes place despite the presence of strong convex curvature and favourable pressure gradient, indicating a clear difference between the near-wall flow and outer region of the boundary layer. Also note from figure 13(*b*) that the location of the peak shifts slightly away from the wall from $0.12\theta_{ref}$ at $x_w/L_c = 1/12$ to $0.2\theta_{ref}$ at $x_w/L_c = 1/2$.

Figure 13(*c*) shows that downstream of the bump summit, K is dominated by increasing adverse pressure gradient for $n/\theta_{ref} < 4$ as evidenced by the significant increase in the peak from 0.012 at $x_w/L_c = 2/3$ to 0.015 at $x_w/L_c = 5/6$. The near-wall profiles of the kinetic energy downstream of the summit at $x_w/L_c = 5/6$ and $11/12$ are noticeably different from those along the upstream convex surface at ($x_w/L_c = 1/6, 1/3, 1/2$) and at $x_w/L_c = 2/3$. As the boundary layer develops along

the upstream convex surface the turbulence kinetic energy in the near-wall region exhibits a consistent streamwise variation with a monotonic and modest increase in the peak value and noticeable reduction further away from the wall to about $n/\theta_{ref} = 4$. The development is quite different downstream of the summit in the region of adverse pressure gradient (e.g. $x_w/L_c = 5/6$) where the profile exhibits a significant increase from the wall to approximately $n/\theta_{ref} = 2$. Note also that the peak values in the profiles do not exhibit a monotonic trend near the downstream concave region. The consistent streamwise variation prior to $x_w/L_c = 2/3$ is a result of the development of an internal layer whose growth is interrupted by the strong adverse pressure gradient on the downstream side of the bump (see also §4.3).

The profiles after the concave-to-flat tangent in figure 13(*d*) show that the near-wall flow ($n < 0.5\theta_{ref}$) evolves differently from that further away from the wall. Immediately after the adverse-to-favourable pressure gradient change at $x_w/L_c = 1$, there is a knee in the profile near $n/\theta_{ref} = 0.1$, which is the beginning of a new inner peak. The outer peak further away is a result of the adverse pressure gradient and concave surface. At $x_w/L_c = 7/6$, the outer peak has decayed significantly and is nearly equal to the new inner peak. As the flow develops further downstream the turbulence kinetic energy decays rapidly for $0.5 < n/\theta_{ref} < 3$, while the peak close to the wall remains nearly unchanged. Note that both the location and level of the inner peak at $x_w/L_c = 3/2$ are not far from those at the inlet shown in figure 13(*a*), indicating a monotonic and relatively rapid return to equilibrium. Overall, the streamwise evolution of K shown in figure 13 demonstrates the existence of the two internal layers near the leading and trailing edge which is consistent with the proposition that the quasi-step increases in C_f are responsible for formation of the internal layers (cf. figure 10*a* in §4.1). Further, the above analysis shows that the development of the upstream internal layer is disrupted shortly after the summit by strong adverse pressure gradient.

The similarity of the present boundary layer to previous flows experiencing detachment, separation, and reattachment, as well as the process of return to equilibrium can be further studied through one of the key descriptors in understanding boundary layer development over curved surfaces, namely, the ratio of the normal to streamwise turbulent stresses (e.g. see Webster *et al.* 1996; Patel & Sotiropoulos 1997). Figure 14 shows the wall-normal profiles of $\langle \overline{u}_n'^2 \rangle / \langle \overline{u}_s'^2 \rangle$. Similar to Baskaran *et al.* (1987), the mild adverse pressure gradient over the upstream flat plate increases streamwise fluctuations while decreasing wall-normal fluctuations, which results in a reduction in $\langle \overline{u}_n'^2 \rangle / \langle \overline{u}_s'^2 \rangle$. In the middle of the upstream concave surface ($x_w/L_c = 1/24$), $\langle \overline{u}_n'^2 \rangle / \langle \overline{u}_s'^2 \rangle$ increases compared to the profile at the onset of curvature because $\langle \overline{u}_s'^2 \rangle$ is reduced by favourable pressure gradient while $\langle \overline{u}_n'^2 \rangle$ is enhanced by the concave curvature (see also Baskaran *et al.* 1987; Barlow & Johnston 1988). Figure 14(*b*) shows that over the upstream convex surface $\langle \overline{u}_n'^2 \rangle / \langle \overline{u}_s'^2 \rangle$ decreases monotonically with streamwise distance. Although not shown here, the wall-normal stress $\langle \overline{u}_n'^2 \rangle$ decreases monotonically with downstream evolution while the streamwise stress $\langle \overline{u}_s'^2 \rangle$ exhibits a development similar to the turbulence kinetic energy (figure 13*b*). This is particularly interesting because it is consistent with the analysis in §4.1 that signatures of the internal layer are more pronounced in the streamwise intensity than wall-normal fluctuations. The reduction of $\langle \overline{u}_n'^2 \rangle$ by convex curvature is then principally responsible for the decrease in $\langle \overline{u}_n'^2 \rangle / \langle \overline{u}_s'^2 \rangle$. Downstream of the bump summit, figure 14(*c*) shows that for $n/\theta_{ref} > 1$, $\langle \overline{u}_n'^2 \rangle / \langle \overline{u}_s'^2 \rangle$ continues to decrease because of the effect of convex curvature. Close to the wall the intermittent reverse flow region caused by the adverse pressure gradient increases wall-normal fluctuations and decreases the streamwise fluctuations (e.g. see Singh & Azad 1995*a*), leading to an increase in this region in $\langle \overline{u}_n'^2 \rangle / \langle \overline{u}_s'^2 \rangle$.

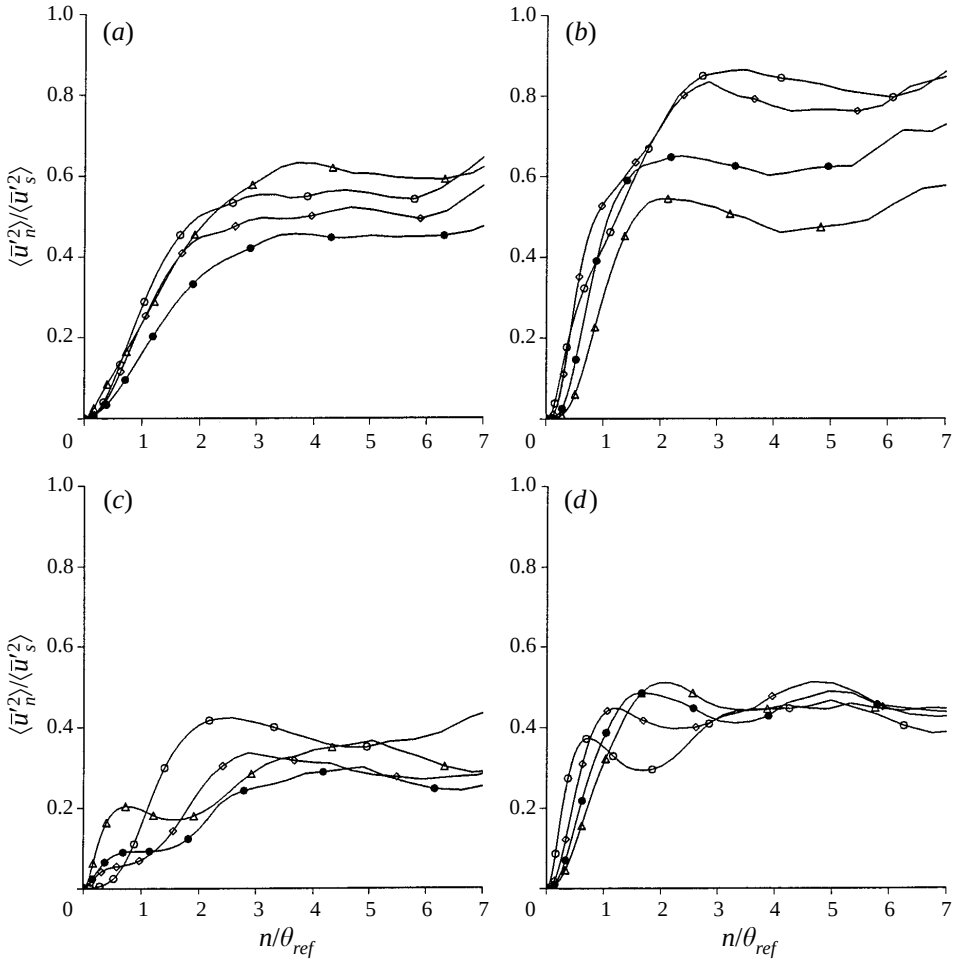

FIGURE 14. Ratio of wall-normal to streamwise turbulent stresses $\langle \overline{u}_n'^2 \rangle / \langle \overline{u}_s'^2 \rangle$, for legend refer to figure 12.

The increase is further enhanced over the concave region due to a relatively large increase in wall-normal fluctuations. Thus, the adverse pressure gradient and concave curvature near the trailing edge strongly distort the boundary layer, as evidenced by the inner peak in $\langle \overline{u}_n'^2 \rangle / \langle \overline{u}_s'^2 \rangle$. Over the downstream flat plate the profiles rapidly relax towards the inlet values. The behaviour of the shear stress and normal stress ratio in the present flow is quite different than that measured in previous experiments on boundary layers experiencing extended convex curvature (in the absence of an external pressure gradient), in which the shear stress is strongly reduced and the normal stresses approach isotropy (e.g. see So & Mellor 1973; Gillis & Johnston 1983; Alving *et al.* 1990). Thus, it should be expected that the relaxation process will be different than the slow recovery observed in boundary layers recovering from convex curvature (see also Webster *et al.* 1996).

In addition to the mean and fluctuating velocities, another important statistical descriptor of the boundary layer is the r.m.s. pressure fluctuations. As discussed in §2.1, since the trace of the SGS stress, τ_{kk}, was not explicitly modelled, the statistics shown in figure 15 include the contribution of the SGS normal stresses. R.m.s. wall pressure

fluctuations are shown in figure 15(*a*). The two peaks in $\overline{p}'_{w,rms}/\frac{1}{2}U_{ref}^2$ are located near the concave-to-convex tangent and the concave-to-flat tangent, respectively. Buckles *et al.* (1984) found in a separated flow over a wavy surface that $\overline{p}'_{w,rms}$ increases at detachment to a maximum just downstream of reattachment (see also Na & Moin 1996). As shown in figure 15(*a*), $\overline{p}'_{w,rms}$ begins to increase over the downstream bump surface at the location of incipient detachment ($x_w/L_c = 0.7$), and attains a maximum just downstream of the location where $\gamma_{+,w} = 0.99$ ($x_w/L_c = 1.02$), in qualitative agreement with the measurements of Buckles *et al.* (1984). Figure 15(*a*) also shows the r.m.s. surface pressure fluctuation normalized by the maximum total shear stress σ_{max}. The values of $\overline{p}'_{w,rms}/\sigma_{max}$ over the upstream flat plate are in general agreement with existing measurements in equilibrium adverse pressure gradient boundary layers (Simpson *et al.* 1987). Simpson, Ghodbane & McGrath (1987) observed that in a separated flat plate flow $\overline{p}'_{w,rms}/\sigma_{max}$ increases to the detachment location and decreases downstream. Figure 15(*a*) shows that $\overline{p}'_{w,rms}/\sigma_{max}$ increases to the position of intermittent transitory detachment, and remains high to about the location of the strongest intermittent backflow before decreasing significantly. The locus of the maximum pressure fluctuations is shown in figure 15(*b*). In the region of intermittent reversal the locus of $\overline{p}'_{rms,max}$ moves away from the wall and coincides with the outer extremities of the region of intermittent backflow. Although not shown here, the loci of the maximum turbulence stresses also coincide with the outer extremities of the intermittent backflow region along the rear bump surface. This is consistent with the observation of Singh & Azad (1995*b*) in flows approaching separation. Thus, the pressure fluctuations in the present boundary layer which exhibits intermittent detachment/reattachment are very similar to previous measurements obtained in detaching/separated/reattaching flows. R.m.s. pressure fluctuations along the wall-normal direction are shown in figure 15(*c*). The profiles over the upstream flat plate ($x_w/L_c = -1/6$) are similar to the DNS results of Spalart (1988) and the experimental results reviewed by Willmarth (1975). Consistent with the behaviour observed in the turbulent stresses, on the downstream flat plate the profiles approach that of the upstream flat plate monotonically.

The spanwise spectra of the surface pressure fluctuations along the bump surface are shown in figure 16. Na & Moin (1996) have shown that when scaled by the r.m.s. wall fluctuation, $p_{w,rms}$, frequency spectra exhibit relatively small scatter in an adverse pressure gradient boundary layer. They also found that the power spectra at high frequencies increase with increasing adverse pressure gradient. The results presented in figure 16(*b*) show similar features. Over the rear bump surface where an adverse pressure gradient prevails the spectra collapse at low wavenumbers, and increase at high wavenumbers with increasing adverse pressure gradient. Figure 16(*a*) shows that over the upstream bump surface the spectra also collapse at low wavenumbers, and decrease at high wavenumbers under the influence of the favourable pressure gradient as the flow approaches the summit.

Additional insights into the similarities and differences between the present intermittent detaching/reattaching boundary layer over the rear surface of the bump and existing measurements on flows exhibiting detachment, separation, and reattachment are illustrated in figure 17. Shown in the figure is the streamwise variation of the relative strength of the large eddies, E_s, as defined by Castro & Bradshaw (1976),

$$E_s = \frac{\langle \overline{q}\,\overline{u}'_n \rangle_{max} - \langle \overline{q}\,\overline{u}'_n \rangle_{min}}{\langle \overline{q} \rangle^{1.5}_{max}}, \tag{4.3}$$

where q is twice the instantaneous turbulence kinetic energy (see also Singh & Azad

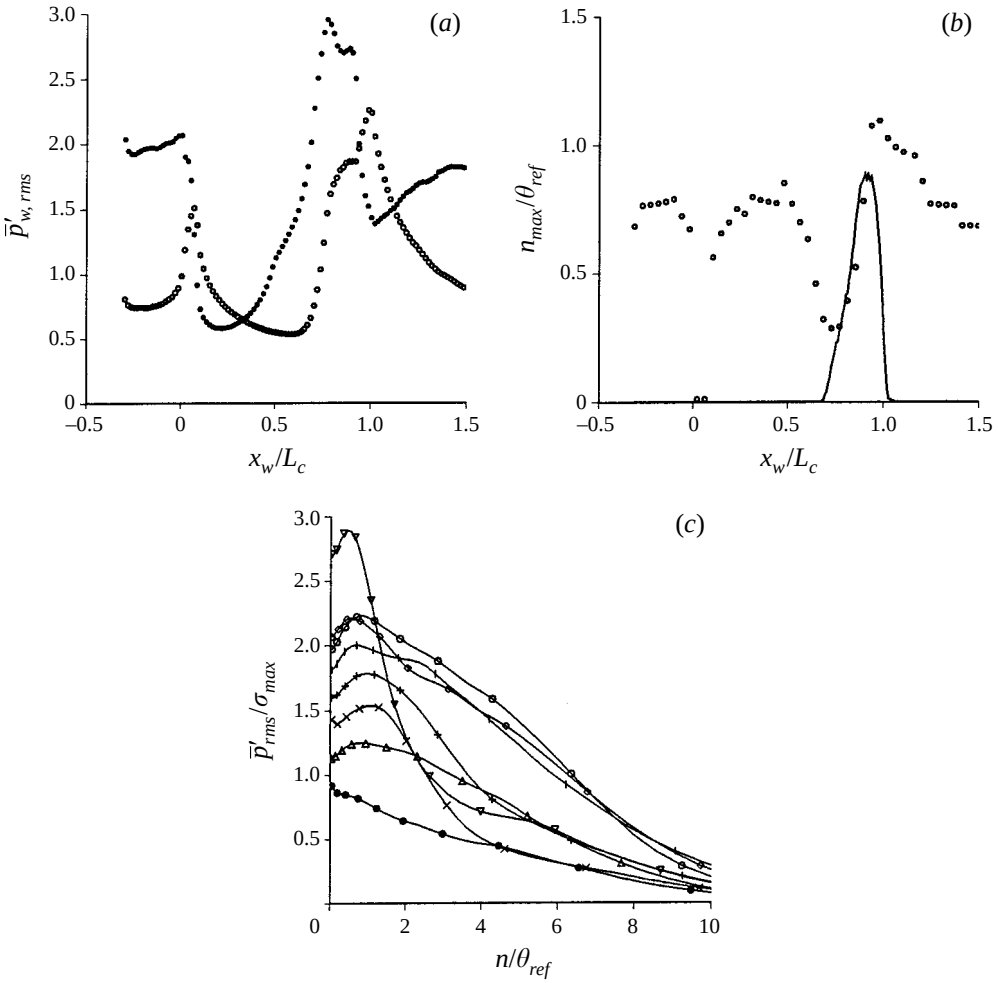

FIGURE 15. R.m.s. pressure fluctuations. (*a*) ○, $10^2\overline{p}'_{w,rms}/\frac{1}{2}U_{ref}^2$, ●, $\overline{p}'_{w,rms}/\sigma_{max}$; (*b*) ○, locus of $\overline{p}'_{rms,max}$; ——, maximum wall-normal extent of intermittent backflow; (*c*) $\overline{p}'_{rms}/\sigma_{max}$, ○, $x_w/L_c = -1/6$; ◇, 0; ●, 1/12; △, 1/2; ∇, 5/6; ×, 1; +, 7/6; |, 3/2.

1995*a*, *b*). Subscripts *min* and *max* refer to local extremities along a wall-normal traverse. Figure 17 shows that there are significant increases in E_s over the upstream and downstream concave surfaces. This is consistent with the conclusion of Barlow & Johnston (1988) that the strength of the large eddies is markedly enhanced by concave curvature. On the trailing flat plate, E_s returns monotonically towards the upstream equilibrium value. It is also found that the trajectory of E_s exhibits a linear dependence on the intermittency backflow factor $\gamma_-(0)$, identical to that reported by Singh & Azad (1995*b*) in intermittently separating flows.

4.3. *Turbulence kinetic energy budget*

The second-order statistics presented in §3 and §4.2 demonstrate behaviour consistent with the proposition discussed in §4.1 that quasi-step increases in C_f induce an internal layer by enhancing the near-wall shear production of $\langle\overline{u}_s'^2\rangle$, K, and $\langle\overline{u}_s'\overline{u}_n'\rangle$. These statistics also convincingly show that development of the upstream internal layer is disrupted shortly downstream of the summit by the strong adverse pressure

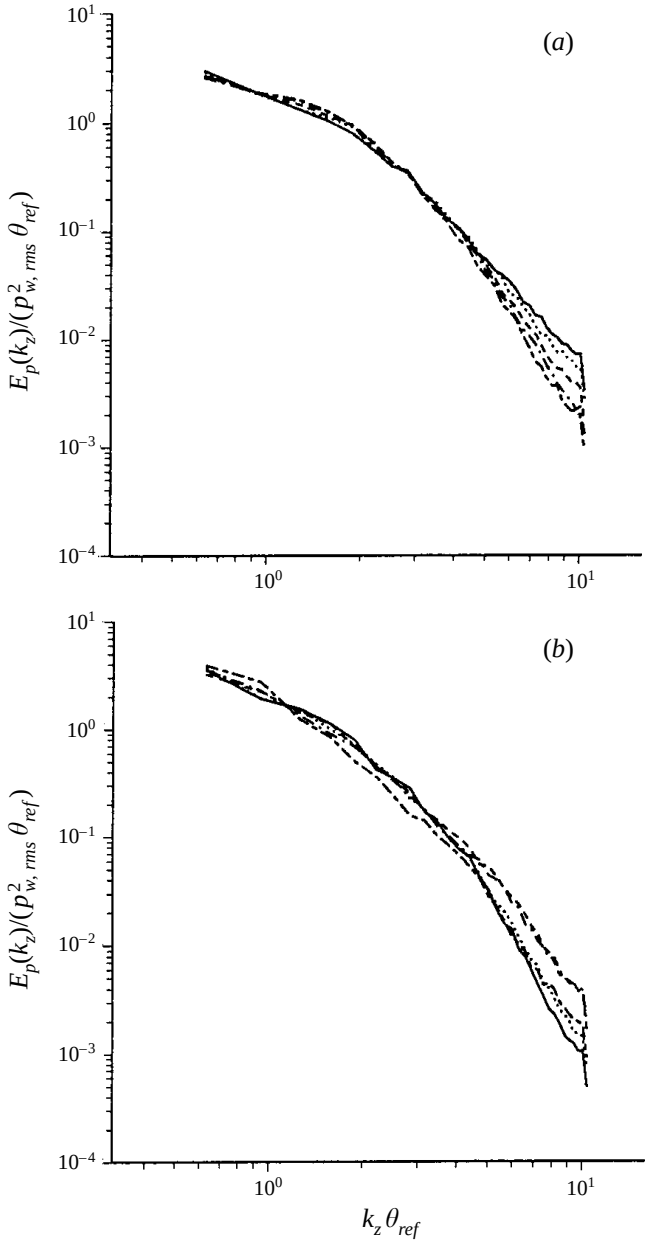

FIGURE 16. Spanwise spectra of surface pressure fluctuations (Case 2): (*a*) upstream bump surface: ——, $x/L_c = 1/12$; · · · · ·, 1/6; – – – – –, 1/4; — · — 1/3, — — — 5/12; (*b*) downstream bump surface: ——, 7/12; · · · · ·, 2/3; – – – – –, 3/4; — · —, 5/6; — — —, 11/12.

gradient. The mean flow and second-order statistics in the region of intermittent detachment/reattachment ($0.7 < x_w/L_c < 1.02$) also exhibit a strong similarity to measurements in detaching/separated/reattaching flows. In addition, profiles of the mean velocity and second-order statistics presented in §3, §4.1 and §4.2 show a rapid return to equilibrium downstream of the bump trailing edge. In this section the response of turbulence kinetic energy to streamwise pressure gradient and surface

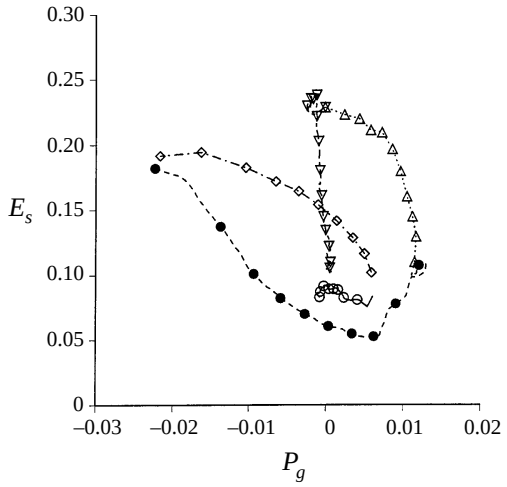

FIGURE 17. Variation of relative strength of large eddies with pressure gradient parameter P_g: ○, upstream flat plate; ◇, upstream concave surface; •, convex surface; △, downstream concave surface; ▽, downstream flat plate.

curvature will be analysed in greater detail using its transport equation for boundary layers in the streamline-normal coordinate system to gain further insights into these important properties.

Following Castro & Bradshaw (1976) (see also Gibson *et al.* 1981; Baskaran, Smits & Joubert 1991), the equation for the resolved kinetic energy can be written as

$$
\begin{aligned}
&-\left[\langle\overline{u}_s\rangle\frac{\partial}{\partial s}+\left(1+\frac{n}{R}\right)\langle\overline{u}_n\rangle\frac{\partial}{\partial n}\right]K-\langle\overline{u}_s'\overline{u}_n'\rangle\left(1+\frac{n}{R}\right)\frac{\partial\langle\overline{u}_s\rangle}{\partial n}\\
&-\langle\overline{u}_s'\overline{u}_n'\rangle\left[\frac{\partial\langle\overline{u}_n\rangle}{\partial s}-\frac{\langle\overline{u}_s\rangle}{R}\right]-(\langle\overline{u}_s'^2\rangle-\langle\overline{u}_n'^2\rangle)\left[\frac{\partial\langle\overline{u}_s\rangle}{\partial s}+\frac{\langle\overline{u}_n\rangle}{R}\right]-\frac{\partial}{\partial s}\left(\langle\overline{p}'\overline{u}_s'\rangle+\langle\tfrac{1}{2}q\overline{u}_s'\rangle\right)\\
&-\frac{\partial}{\partial n}\left[\left(1+\frac{n}{R}\right)\left(\langle\overline{p}'\overline{u}_n'\rangle+\langle\tfrac{1}{2}q\overline{u}_n'\rangle\right)\right]+D_1=0. \qquad (4.4)
\end{aligned}
$$

The first four terms on the left-hand-side of (4.4) can be interpreted as advection, shear production, curvature production, and normal stress production, respectively; the next two terms can be viewed together as turbulent diffusion; the last term D_1 contains primarily dissipation plus viscous diffusion and terms resulting from the filtering operation (e.g. see Moin & Kim 1982). As shown by Baskaran *et al.* (1987), the normal stress production term can be written as $(\langle\overline{u}_s'^2\rangle-\langle\overline{u}_n'^2\rangle)(1+n/R)\partial\langle\overline{u}_n\rangle/\partial n$ using the continuity equation. The effect of the streamwise pressure gradient can also be linked to $\partial\langle\overline{u}_n\rangle/\partial n$. For instance, $\partial\langle\overline{u}_s\rangle/\partial s<0$ in a decelerated two-dimensional incompressible flow due to adverse pressure gradient has $\partial\langle\overline{u}_n\rangle/\partial n>0$. Thus, as also discussed by Smits & Wood (1985), changes in normal stress production can be interpreted as caused by changes in streamwise pressure gradient.

The terms appearing in (4.4) at 12 streamwise stations are shown in figure 18. At the inlet, the LES pre-computation yields the budgets of a canonical zero-pressure-gradient boundary layer (e.g. see Spalart 1988). At the onset of curvature ($x_w/L_c=0$) the positive normal stress contribution due to adverse pressure gradient becomes comparable to the shear production (figure 18*b*). This is consistent with the increase in the peak kinetic energy shown in figure 13*a*. In the middle of the upstream concave surface ($x_w/L_c=1/24$) immediately following the step change in pressure gradient

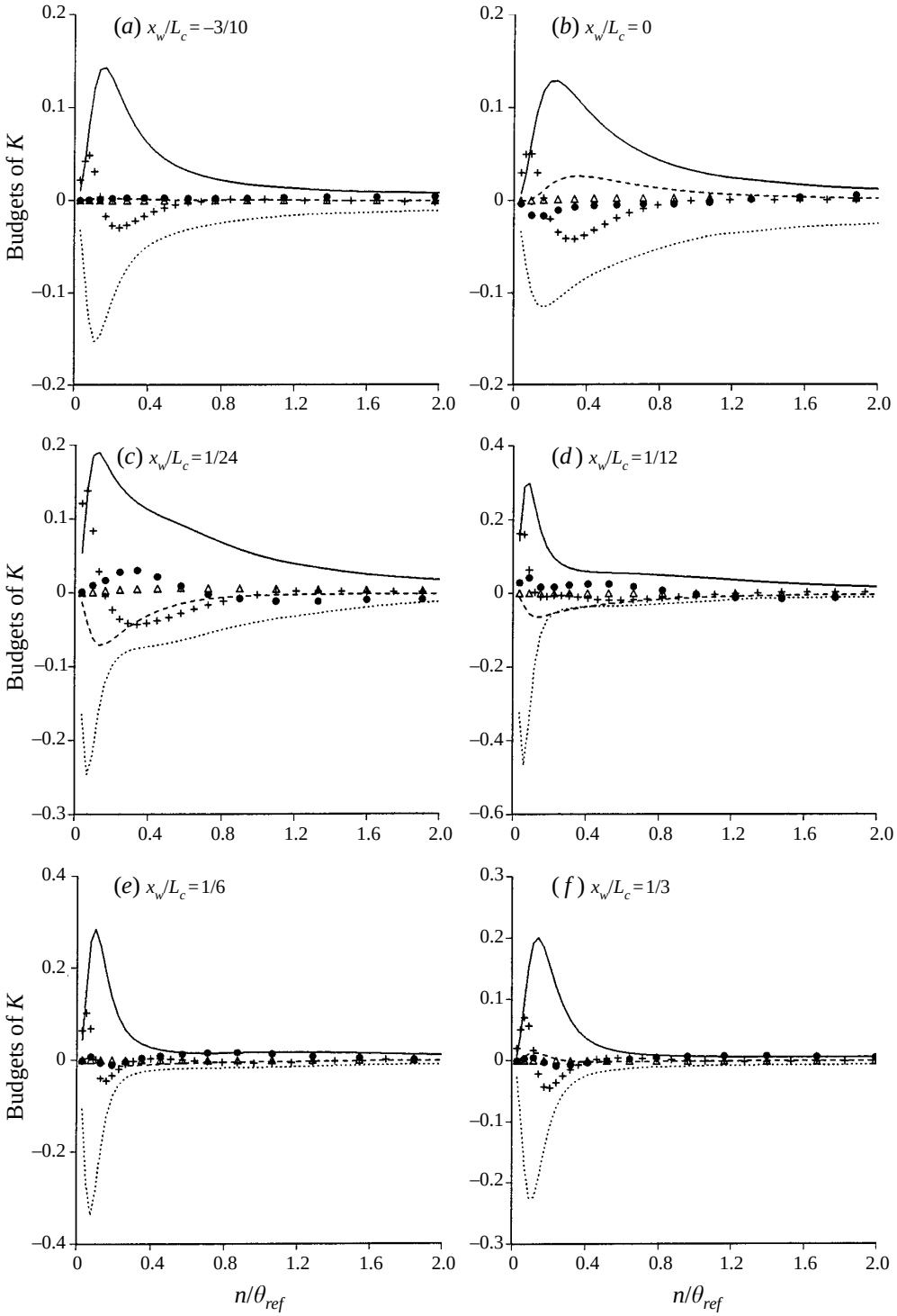

FIGURE 18(*a–f*). For caption see facing page.

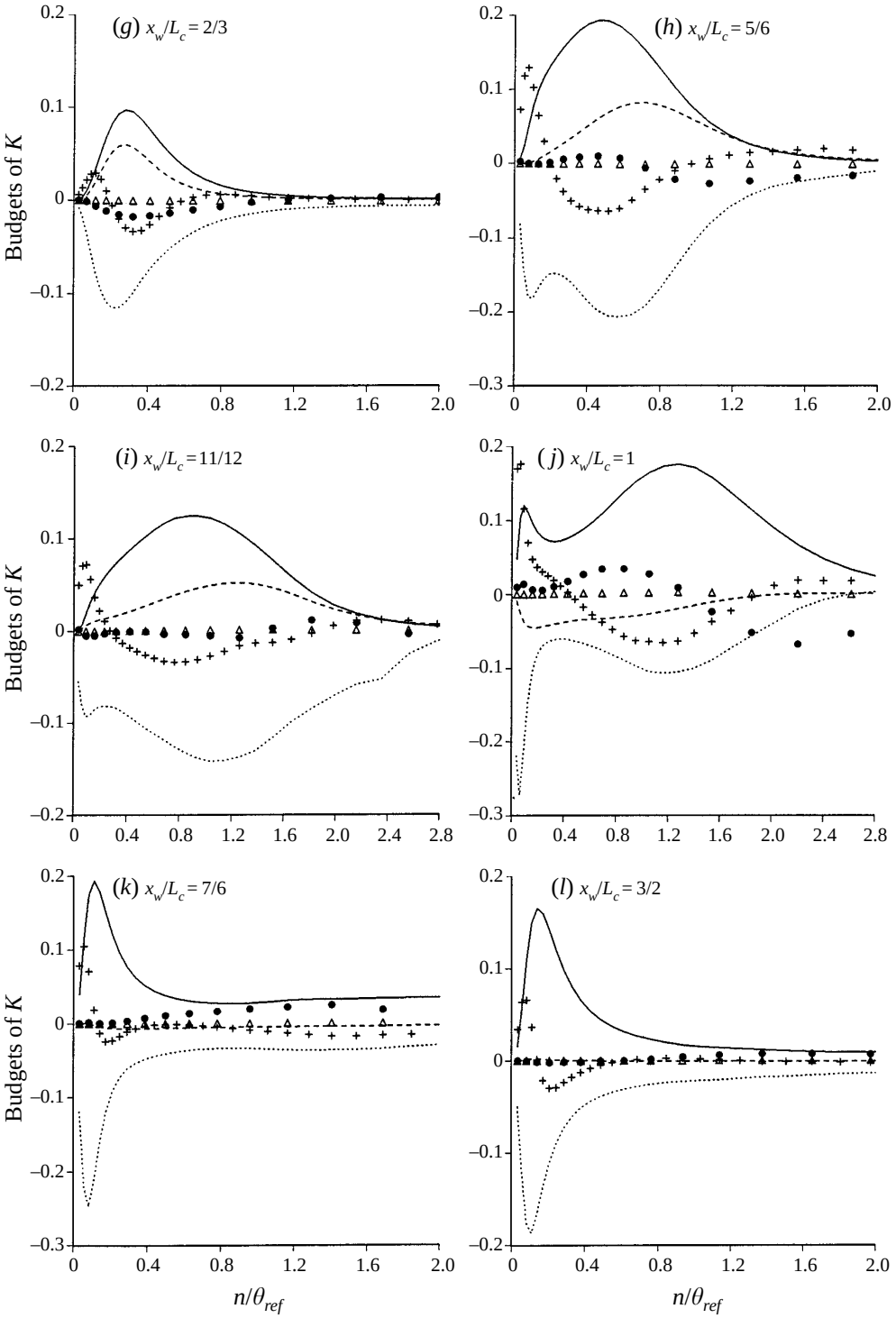

FIGURE 18. Turbulence kinetic energy budgets: •, advection; ——, shear production; – – – –, normal stress production; △, curvature production; +, turbulent diffusion; · · · ·, difference; all terms multiplied by $10^2\theta_{ref}/U_{ref}^3$.

from adverse to favourable, the normal stress production is significantly negative (figure 18*c*). Knee points appear in the profiles of shear production and dissipation and the peaks are located closer to the wall as compared to the profiles at $x_w/L_c = 0$. Near the wall over the upstream convex surface ($x_w/L_c = 1/12,\ 1/6,\ 1/3$), shear production and dissipation are nearly in balance and are also much larger than in the outer part of the layer. As the flow approaches the summit the peaks in shear production and dissipation gradually shift outward. As discussed in Townsend (1976), a boundary layer subjected to abrupt changes in external conditions may establish an inner region in which an energy equilibrium between production and dissipation is established, and motion in the inner region is determined primarily by local conditions. Britter, Hunt & Richards (1981) also noted that the evolution of a boundary layer flowing over a Gaussian hill can be considered using a two-layer model, i.e. an inner energy-equilibrium region governed mostly by local conditions and an outer region primarily under the influence of inviscid effects. The large shear production and dissipation below $n/\theta_{ref} = 0.2$ shown in figure 18(*d–f*) further support the fact that the response of the boundary layer occurs through development of an internal layer. As indicated in figure 18(*c*), the origin of this inner region can be traced to the profiles upstream of the concave-to-convex tangent (after the adverse-to-favourable pressure gradient transition), i.e. knee points and the inward shift in the peak in the profiles of the shear production and dissipation. Also note in figure 18(*e*) that the production beyond $n/\theta_{ref} = 0.4$ is nearly zero due to the stabilizing effect of convex curvature and favourable pressure gradient.

The profiles of the budget terms over the downstream surface shown in figure 18(*g–i*) are not similar to those over the upstream convex surface in which there exists an inner energy-equilibrium region. The locations of the peak in shear production and dissipation are displaced away from the wall by the strong adverse pressure gradient; the contribution from normal stress production is also comparable to shear production. Corresponding to the displacement in the peak production are the increased levels of kinetic energy away from the wall (cf. figure 13). Figure 18(*g–i*) also shows that in the region of intermittent flow reversal, the turbulent diffusion term becomes large, which is similar to the report by Simpson *et al.* (1981*b*) that as separation is approached turbulent diffusion becomes increasingly significant. Since shear production and dissipation are no longer the only dominant terms in the kinetic energy balance, the strong adverse pressure gradient along the downstream surface has interrupted the development of the internal layer. This is consistent with the distinctly different profiles of the kinetic energy upstream and downstream of $x_w/L_c = 2/3$ shown in figure 13, which further demonstrates that the inner region which develops over the upstream surface has been interrupted by the strong adverse pressure gradient shortly after the bump summit.

At $x_w/L_c = 1$ where the concave-to-flat tangent is located and the adverse-to-favourable pressure gradient transition takes place, favourable pressure gradient makes a significant negative contribution to the transport of turbulence kinetic energy. Note also that there is strong similarity in the inner-region ($n/\theta_{ref} < 0.2$) profiles shown in figure 18(*j*) and those in figure 18(*c*), with the peaks in shear production and dissipation located very close to the wall and knee points apparent in the profiles. From $x_w/L_c = 1$ to 3/2, the locations of the peak shear production and dissipation shift slowly outward. This behaviour is again consistent with the formation and growth of a new internal layer. Over the downstream flat plate, production for $n/\theta_{ref} > 0.5$ becomes increasingly negligible compared to that in the inner region as the flow relaxes from the removal of perturbations in curvature and pressure gradient.

By $x_w/L_c = 3/2$, the budgets have nearly asymptoted to those at the inlet shown in figure 18(*a*). The decay of kinetic energy away from the wall corresponding to the decrease in production in this region and re-establishment of inner shear production coincides with the rapid recovery of the kinetic energy shown in figure 13(*d*).

5. Model response

Most information on characteristics of dynamic models has been acquired in canonical flows such as isotropic turbulence and turbulent channel flow (e.g. see Meneveau *et al.* 1996). As shown in §4, perturbations in pressure gradient and surface curvature cause a strong distortion of boundary layer turbulence, i.e. suppression over the summit, amplification near the trailing edge and rapid recovery along the downstream plate. The flow over the bump then provides a unique platform for the examination of model response to external perturbations in a well-defined non-equilibrium boundary layer.

One of the most interesting features of the dynamic eddy viscosity model is that, while the model is mostly dissipative, the quantity $L_{ij}M_{ij}$ which appears in the numerator of (2.13) can be positive or negative. On average $L_{ij}M_{ij}$ is negative and the coefficient C is positive, reflecting the fact that on the average the small scales are dissipative. Piomelli (1993) and Mason (1994) have shown that the effect of regions where $L_{ij}M_{ij}$ is positive reduces the level of the coefficient thereby accounting for subgrid-scale backscatter, albeit in an average sense. The positive and negative contributions to the model coefficient can be expressed as

$$C_+ = -\frac{1}{4}\frac{\langle L_{ij}M_{ij} - |L_{ij}M_{ij}|\rangle}{\langle M_{ij}M_{ij}\rangle}, \qquad C_- = -\frac{1}{4}\frac{\langle L_{ij}M_{ij} + |L_{ij}M_{ij}|\rangle}{\langle M_{ij}M_{ij}\rangle}, \tag{5.1}$$

where $C_+ > 0$ and corresponds to forward transfer of energy (from large to small scales) while $C_- < 0$ corresponds to a backscatter of energy from the SGS to resolved motions (see Piomelli 1993; Najjar & Tafti 1996). Figure 19 shows the ratio of the model coefficient C to the Smagorinsky constant $C_s = 0.1^2$ along six representative wall-normal traverses. Also shown are the related positive and negative contributions from (5.1). At the inflow boundary $x/L_c = -1/3$ the profiles of C, C_+, and C_- are similar to those in fully developed channel flow (Piomelli 1993). At the onset of curvature $x/L_c = 0$, turbulence levels are enhanced by the relatively strong adverse pressure gradient and the front concave surface (see figure 13*a*). As indicated in figure 19(*b*), the model responds by yielding a coefficient C about two times larger in the near-wall region than that at the inlet. At the bump summit ($x/L_c = 1/2$), convex curvature and favourable pressure gradient suppress turbulent fluctuations causing a significant decrease in C. At the trailing edge the strong adverse pressure gradient and concave curvature significantly elevate turbulence levels and the peaks of turbulence kinetic energy and shear stress are located far from the wall (cf. figure 13*c*, see also Webster *et al.* 1996). In response, at $x/L_c = 1$ the dynamic model yields a coefficient C nearly five times larger than that at the inflow boundary. The positive and negative contributions C_+ and C_- show similar increases. Over the downstream flat plate the profiles rapidly return to those at the upstream reference station.

Figure 20 shows the percentage of points where the product $L_{ij}M_{ij}$ takes positive values (i.e. locally negative C). These profiles exhibit a strikingly close dependence on the enhanced/suppressed turbulence levels due to external perturbations in streamwise pressure gradient and surface curvature. Using the profile in figure 20(*a*) at the inlet as a reference, the weak adverse pressure gradient over the upstream flat plate has a

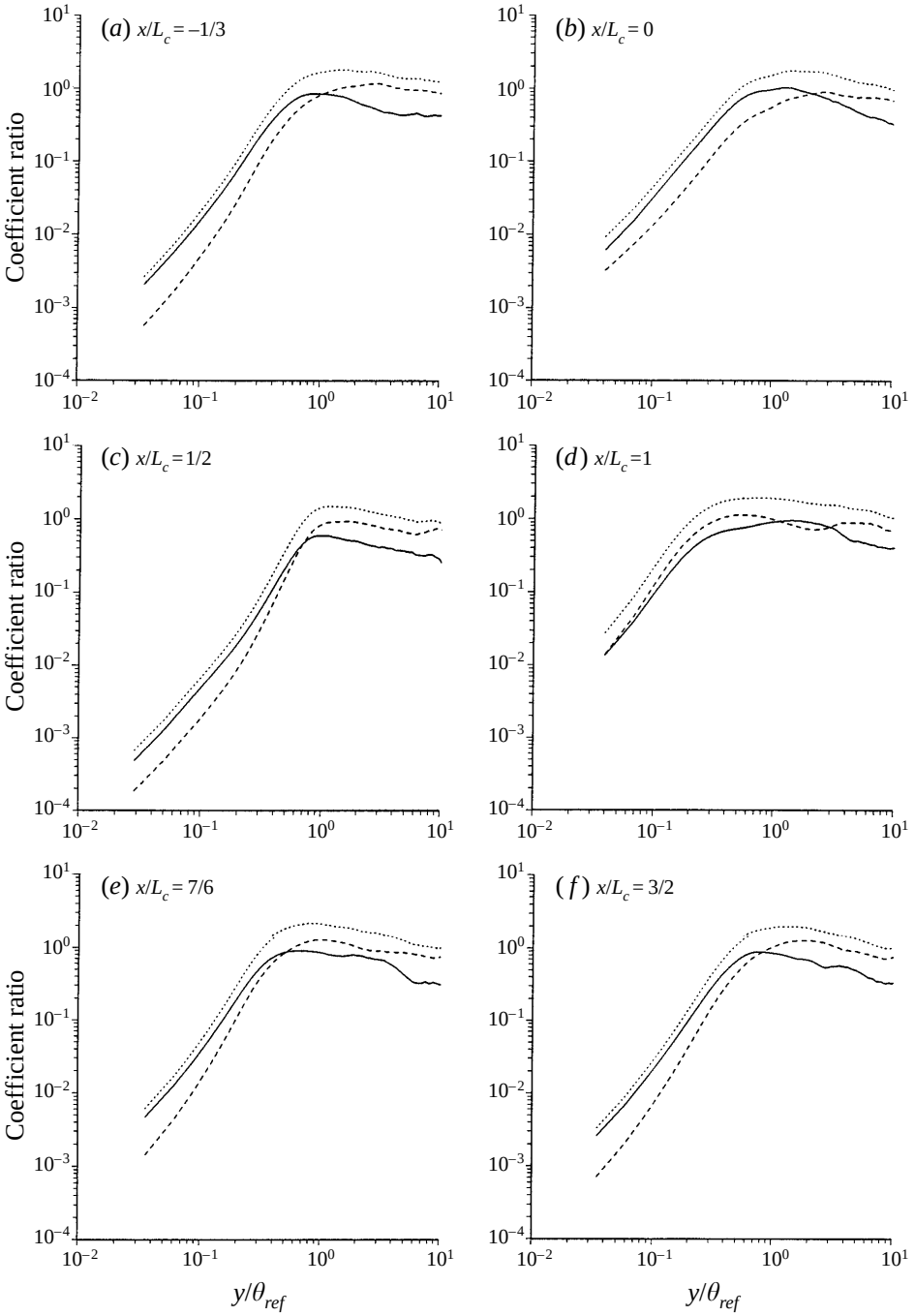

FIGURE 19. Model coefficient; ——, C/C_s; · · · · ·, forward contribution C_+/C_s; – – – –, backward contribution $-C_-/C_s$ (profiles shown are time averages).

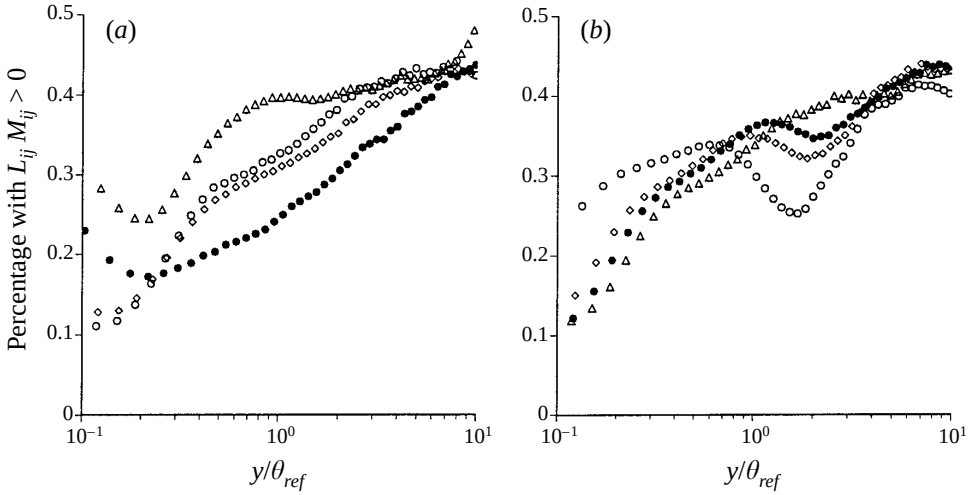

FIGURE 20. Percentage of points where $L_{ij}M_{ij} > 0$ (corresponding to locally negative C). (a), ○, $x/L_c = -1/3$; ◇, $-1/6$; ●, 0; △, 1/2; (b) ○, $x/L_c = 1$; ◇, 13/12; ●, 7/6; △, 3/2.

mild effect as seen in the small differences in the profiles at $x/L_c = -1/3$ and $-1/6$. At the onset of curvature, $x/L_c = 0$, turbulence fluctuation levels are enhanced by concave curvature and adverse pressure gradient (see figure 13a). At this location the percentage of points where $L_{ij}M_{ij} > 0$, corresponding to a locally negative coefficient, decreases. Thus, while both the (average) positive and negative contributions to the coefficient increase at this location (figure 19), there is a relatively larger forward transfer of energy and decreased likelihood of backscatter. In contrast, at the bump summit where the coefficient is reduced by the stabilizing effects of favourable pressure gradient and convex curvature, the model predicts an increasingly larger fraction of points where the coefficient is locally negative. Since the small scales evolve on shorter time scales, their response to changes in external conditions will be more rapid than for the large scales. The relative increase in reverse flow of energy is then possibly one consequence of the more rapid adjustment of the smaller scales. In the near-wall region, the percentage of points corresponding to negative C at the summit has increased by nearly a factor of two compared to the bump leading edge.

As may be observed in figure 20(b), the behaviour of the model along the rear surface of the bump is extremely interesting. In this region turbulent fluctuation levels have been substantially increased and peak values displaced away from the wall by adverse pressure gradient (see figure 13c). The relative increase in the energy content of the smallest resolved scales leads to a stronger transfer of energy to SGS motions. A deficit in the profile is apparent at the trailing edge of the bump, which is correlated with peak values of the kinetic energy, K, as well as production and dissipation of K (see §4.3). While the SGS dissipation also increases (see figure 22), the dynamic model predicts a greater likelihood of energy transfer from large to small scales. As the boundary layer returns to equilibrium over the trailing flat plate, the profiles shown in figure 20(b) also recover rapidly, coinciding with the decay of elevated turbulence levels in the outer region (cf. figure 13d). At the last station $x/L_c = 3/2$ the profile has nearly asymptoted to that at $x/L_c = -1/3$.

As discussed in §2.1, a clipping function is applied to (2.13) to remove negative model coefficients following spanwise averaging. One measure of the effect of such an operation is the ratio of model coefficients obtained with and without clipping, which

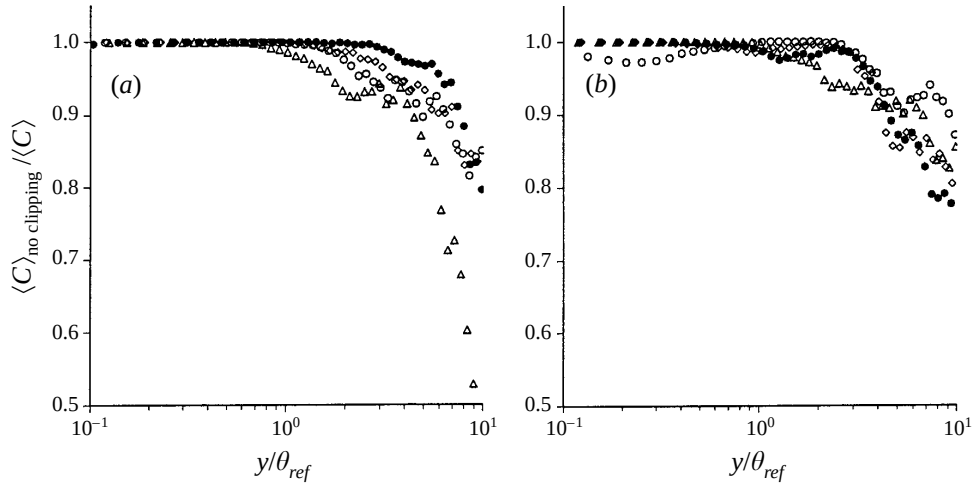

FIGURE 21. Ratio of model coefficient with clipping applied to negative $-\langle L_{ij}M_{ij}\rangle_z$ to model coefficient used in the LES. (*a*) ○, $x/L_c = -1/3$; ◇, $-1/6$; •, 0; △, 1/2; (*b*), ○; $x/L_c = 1$, ◇, 13/12; •, 7/6; △, 3/2.

is defined as

$$\frac{\langle C\rangle_{\text{no clipping}}}{\langle C\rangle} = \frac{\langle -\langle L_{ij}M_{ij}\rangle/2\langle M_{ij}M_{ij}\rangle\rangle_t}{\langle max\{0, -\langle L_{ij}M_{ij}\rangle/2\langle M_{ij}M_{ij}\rangle\}\rangle_t}, \tag{5.2}$$

where t denotes averaging over time. Because negative values (if any) following spanwise averaging will lower the model coefficient, $\langle C\rangle_{\text{no clipping}} \leqslant \langle C\rangle$. Figure 21 shows the profiles of (5.2) at eight streamwise locations from the Case 2 simulation. Figure 21(*a*) and figure 21(*b*) both show that from the wall to approximately one momentum thickness, virtually no clipping of the model coefficient was necessary in the region where most of the turbulence production takes place. This is consistent with other studies in which averaging over directions of statistical homogeneity yields model coefficients which are rarely negative (e.g. see Ghosal *et al.* 1995). Between $y/\theta_{ref} = 1$ and 2, negative contributions to the model coefficient account for roughly 5% of $\langle C\rangle$, again indicating that the overall effect of clipping is small. At the boundary layer edge the magnitude of the negative contributions increases to about 30%, suggesting a rather substantial effect of clipping on the calculated model coefficient in this region. However, it must be noted that the mean strain rate is weak in the outer layer and the SGS dissipation (hence the role of the model) becomes increasingly small near the boundary layer edge. Thus, based upon the results shown in figure 21, clipping the negative occurrences of $-\langle L_{ij}M_{ij}\rangle(x, y, t)$ is unlikely to result in any significant difference between the present results and those in which no clipping is performed.

Perhaps the most important aspect of the model is providing the correct dissipation, ε_{sgs}, of energy from large to small scales. Analogous to the decomposition of the model coefficient above, the SGS dissipation can be expressed as

$$\varepsilon_{sgs} = \varepsilon_+ + \varepsilon_-, \qquad \varepsilon_+ = -\langle C_+\overline{\Delta}^2|\overline{S}|^3\rangle, \qquad \varepsilon_- = -\langle C_-\overline{\Delta}^2|\overline{S}|^3\rangle. \tag{5.3}$$

Shown in figure 22 are profiles of the total SGS dissipation, in addition to the positive (ε_+) and negative (ε_-) contributions along six representative vertical traverses. Similar to the behaviour observed in figure 19, the levels of SGS dissipation increase/decrease in response to the external perturbations in pressure gradient and curvature, i.e. substantial suppression of ε_{sgs} at the bump summit, significant increase at the trailing

edge, and rapid return to the equilibrium profiles at the inlet along the trailing flat plate. Figure 22 shows that in regions where the SGS dissipation is large, there is a tendency for a relatively larger increase in ε_+ compared to ε_-. The strong correlation between model properties and the state of the flow illustrated in figures 19–22 is striking and provides further evidence of the ability of the dynamic model to properly reflect changes in the spectral content of the turbulence.

6. Summary

Large-eddy simulation of the spatially developing turbulent boundary layer over a bump has been performed. A canonical flat-plate boundary layer introduced at the inflow boundary to the bump was generated from a separate pre-computation. The flow is then subject to perturbations in streamwise pressure gradient and surface curvature and exhibits a strong departure from equilibrium along the bump surface, eventually relaxing towards equilibrium over the downstream flat plate. In general, LES predictions of the mean flow and turbulence intensities are in good agreement with the data of Webster *et al.* (1996), with the greatest discrepancy occurring in prediction of peak shear stress levels along the rear bump surface.

LES results were utilized for investigation of three related issues relevant to non-equilibrium boundary layers, i.e. the existence, cause and development of internal layers due to curvature discontinuity, the mechanism governing the return to equilibrium over the trailing flat plate, and the characteristics of a flow experiencing a cycle of intermittent detachment and intermittent reattachment. LES results confirm the existence of internal layers over the bump upstream surface and the trailing flat plate found previously in the experiments of Baskaran *et al.* (1987) and Webster *et al.* (1996). Analysis shows that the cause of the internal layers is the quasi-step increase in skin friction occurring near the bump leading and trailing edge which selectively modifies near-wall shear production of turbulent stresses. This also explained several features associated with internal layers arising from curvature change found in previous experiments such as the absence of knee points in spanwise and wall-normal fluctuations at locations where the streamwise intensity displays distinct knees (Webster *et al.* 1996), and the absence of an internal layer when the skin-friction increase is rather gradual (Alving *et al.* 1990). The present results also clearly show that the growth of the upstream internal layer is disrupted shortly downstream of the bump summit by the strong adverse pressure gradient, rather than developing independently from the parent boundary layer to the downstream curvature discontinuity or separation. The boundary layer over the rear surface is unique in that it completes a cycle of intermittent detachment and reattachment but without mean flow separation. The properties of the flow in this region are qualitatively similar to those previously found in detaching/separated/reattaching flows. The driving mechanism behind the rapid return to equilibrium over the trailing flat plate found in the experiments of Webster *et al.* (1996) has been explained using the turbulence kinetic energy budgets and occurs through the simultaneous decay of the elevated turbulence shear production away from the wall and the uninterrupted growth of an inner region characterized by an equilibrium between shear production and dissipation.

The response of the dynamic eddy viscosity model of Germano *et al.* (1991) to the simultaneous perturbations in streamwise pressure gradient and surface curvature was also examined. Corresponding to suppressed/enhanced turbulence levels the model yields substantially different values of the model coefficient and SGS dissipation. The percentage of points where the coefficient is predicted to be locally negative is

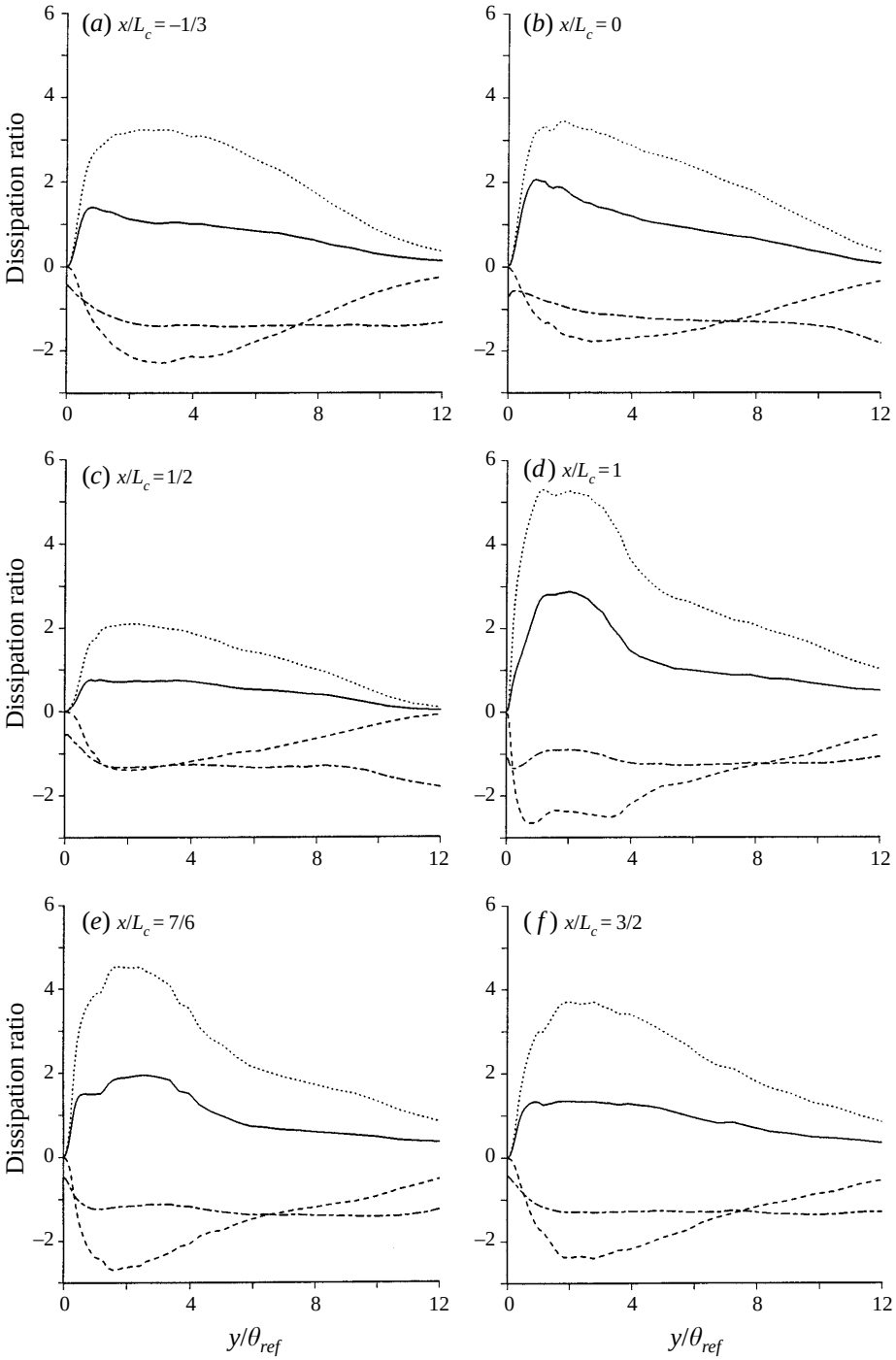

FIGURE 22. SGS dissipation. ——, $\varepsilon_{sgs}/\varepsilon_v$; · · · · ·, forward contribution $\varepsilon_+/\varepsilon_v$; – – – –, backward contribution $\varepsilon_-/\varepsilon_v$; — · —, $2\varepsilon_-/\varepsilon_+$.

correlated with state of the flow. In regions where the flow is stabilized the relative contribution of backscatter increases, while in regions where turbulence levels are increased there is a relative increase in the transfer of energy from large to small scales. Because dynamic models sample the flow field, even eddy viscosity formulations are capable of accounting for some non-equilibrium effects. These aspects of the model cannot be easily inferred from previous work in canonical, equilibrium turbulent flows and motivate further application of the model to the complex flows of engineering interest.

This work is supported by the US Office of Naval Research (Grant Numbers N00014-94-1-0047 and N00014-94-1-1053, Program Officer: Dr L. Patrick Purtell). The authors gratefully acknowledge valuable discussions with Professor J. Eaton, Professor T. Lund, Professor D. Webster, and Mr D. Degraaff. Most of the simulations were performed on the Cray C90 and T90 at the US Department of Defense High Performance Computing Major Shared Resource Centers (CEWES and NAVO). Additional computing time was supplied by National Science Foundation Pittsburgh Supercomputing Center and Cornell Theory Center.

REFERENCES

Akselvoll, K. & Moin, P. 1995 Large-eddy simulation of turbulent confined coannular jets and turbulent flow over a backward facing step. *Rep.* TF-63. Mechanical Engineering Department, Stanford University.

Akselvoll, K. & Moin, P. 1996 Large-eddy simulation of turbulent confined coannular jets. *J. Fluid Mech.* **315**, 387–411.

Alving, A. E., Smits, A. J. & Watmuff, J. H. 1990 Turbulent boundary layer relaxation from convex curvature. *J. Fluid Mech.* **211**, 529–556.

Bandyopadhyay, P. R. & Ahmed, A. 1993 Turbulent boundary layers subjected to multiple curvatures and pressure gradients. *J. Fluid Mech.* **246**, 503–527.

Barlow, R. S. & Johnston, J. P. 1988 Structure of a turbulent boundary layer on a concave surface. *J. Fluid Mech.* **191**, 137–176.

Baskaran, V., Smits, A. J. & Joubert, P. N. 1987 A turbulent flow over a curved hill. Part 1. Growth of an internal boundary layer. *J. Fluid Mech.* **182**, 47–83.

Baskaran, V., Smits, A. J. & Joubert, P. N. 1991 A turbulent flow over a curved hill. Part 2. Effects of streamline curvature and streamwise pressure gradient. *J. Fluid Mech.* **232**, 377–402.

Bradshaw, P. & Galea, P. V. 1967 Step induced separation of a turbulent boundary layer in incompressible flow. *J. Fluid Mech.* **27**, 111–130.

Britter, R. E., Hunt, J. C. R. & Richards, K. J. 1981 A Reynolds stress model for near-wall turbulence. *Q. J. R. Met. Soc.* **107**, 91–110.

Buckles, J., Hanratty, T. J. & Adrian, R. J. 1984 Turbulent flow over large-amplitude wavy surfaces. *J. Fluid Mech.* **140**, 27–44.

Castro, I. P. & Bradshaw, P. 1976 The turbulence structure of a highly curved mixing layer. *J. Fluid Mech.* **73**, 265–304.

Choi, H., Moin, P. & Kim, J. 1993 Direct numerical simulation of turbulent flow over riblets. *J. Fluid Mech.* **255**, 503–539.

Germano, M. 1992 Turbulence: the filtering approach. *J. Fluid Mech.* **238**, 325–336.

Germano, M., Piomelli, U., Moin, P. & Cabot, W. H. 1991 A dynamic subgrid-scale eddy viscosity model. *Phys. Fluids* A **3**, 1760–1765.

Ghosal, S., Lund, T. S., Moin, P. & Akselvoll, K. 1995 A dynamic localization model for large-eddy simulation of turbulent flows. *J. Fluid Mech.* **286**, 229–255.

Ghosal, S. & Moin, P. 1995 The basic equations for the large eddy simulation of turbulent flows in complex geometry. *J. Comput. Phys.* **118**, 24–37.

Gibson, M. M., Jones, W. P. & Younis, B. A. 1981 Calculation of turbulent boundary layers on curved surfaces. *Phys. Fluids* **24**, 386–395.

Gillis, J. C. & Johnston, J. P. 1983 Turbulent boundary layer flow and structure on a convex wall and its redevelopment on a flat wall. *J. Fluid Mech.* **135**, 123–153.

Hoffmann, P. H, Muck, K. C. & Bradshaw, P. 1985 The effect of concave surface curvature on turbulent boundary layers. *J. Fluid Mech.* **161**, 371–403.

Horiuti, K. 1993 A proper velocity scale for modeling subgrid-scale eddy viscosity in large eddy simulation. *Phys. Fluids* A **5**, 146–157.

Jiménez, J. 1995 On why dynamic subgrid-scale models work. *Annual Research Briefs*, pp. 25–34. Center for Turbulence Research, Stanford University.

Lesieur, M. & Metais, O. 1996 New trends in large-eddy simulation of turbulence. *Ann. Rev. Fluid Mech.* **28**, 45–82.

Lilly, D. K. 1992 A proposed modification of the Germano subgrid-scale closure method. *Phys. Fluids* **4**, 633–635.

Lund, T. S. & Moin, P. 1996 Large eddy simulation of a boundary layer on a concave surface. *Intl J. Heat Fluid Flow* **17**, 290–295.

Lund, T. S., Wu, X. & Squires, K. D. 1996 On the generation of turbulent inflow conditions for boundary layer simulations. *Annual Research Briefs*, Center for Turbulence Research, pp. 281-295, Stanford University.

Lund, T. S., Wu, X. & Squires, K. D. 1998 Generation of turbulent inflow data for spatially-developing boundary layer simulations. *J. Comput. Phys.* **140**, 233–258.

Mason, P. J. 1994 Large-eddy simulation: A critical review of the technique. *Q. J. R. Met. Soc.* **120**, 1–26.

Meneveau, C., Lund, T. S. & Cabot, W. 1996 A Lagrangian dynamic subgrid-scale model of turbulence. *J. Fluid Mech.* **319**, 353–385.

Moin, P. & Kim, J. 1982 Numerical investigation of turbulent channel flow. *J. Fluid Mech.* **118**, 341–377.

Moin, P., Squires, K. D., Lee, S. & Cabot, W. 1991 A dynamic subgrid-scale model for compressible turbulence and scalar transport. *Phys. Fluids* A **3**, 2746–2757.

Moser, R. D. & Moin, P. 1987 The effect of curvature in wall-bounded turbulent flows. *J. Fluid Mech.* **175**, 479–510.

Muck, K. C., Hoffmann, P. H. & Bradshaw, P. 1985 The effect of convex surface curvature on turbulent boundary layers. *J. Fluid Mech.* **161**, 347–369.

Na, Y. & Moin, P. 1996 Direct numerical simulation of turbulent boundary layers with adverse pressure gradient and separation. *Rep.* TF-68. Mechanical Engineering Department, Stanford University.

Najjar, F. M. & Tafti, D. K. 1996 Study of discrete test filters and finite difference approximations for the dynamic subgrid-scale stress model. *Phys. Fluids* **8**, 1076–1087.

Patel, V. C. 1965 Calibration of the Preston tube and limitations on its use in adverse pressure gradients. *J. Fluid Mech.* **23**, 185–208.

Patel, V. C. & Sotiropoulos, F. 1997 Longitudinal curvature effects in turbulent boundary layers. *Prog. Aero. Sci.* **33**, 1–70.

Perry, A. E. & Schofield, W. H. 1973 Mean velocity and shear stress distributions in turbulent boundary layers. *Phys. Fluids* **16**, 2068–2074.

Piomelli, U. 1993 High Reynolds number calculations using the dynamic subgrid-scale stress model. *Phys. Fluids* A **5**, 1484–1490.

Piomelli, U. & Liu, J. 1995 Large eddy simulation of rotating channel flows using a localized dynamic model. *Phys. Fluids* **7**, 839–848.

Rosenfeld, M., Kwak, D. & Vinokur, M. 1991 A fractional step solution method for the unsteady incompressible Navier-Stokes equations in generalized coordinate systems. *J. Comput. Phys.* **94**, 102–137.

Samuel, A. E. & Joubert, P. N. 1974 A boundary layer developing in an increasingly adverse pressure gradient. *J. Fluid Mech.* **66**, 481–505.

Simpson, R. L. 1989 Turbulent boundary layer separation. *Ann. Rev. Fluid Mech.* **21**, 205–234.

Simpson, R. L., Chew, Y. T. & Shivaprasad, B. G. 1981*a* The structure of a separating turbulent boundary layer. Part 1. Mean flow and Reynolds stresses. *J. Fluid Mech.* **113**, 23–51.

Simpson, R. L., Chew, Y. T. & Shivaprasad, B. G. 1981*b* The structure of a separating turbulent boundary layer. Part 2. High-order turbulence results. *J. Fluid Mech.* **113**, 53–73.

Simpson, R. L., Ghodbane, M. & McGrath, B. E. 1987 Surface pressure fluctuations in a separating turbulent boundary layer. *J. Fluid Mech.* **177**, 167–186.

Singh, R. K. & Azad, R. S. 1995*a* Structure of turbulence in an incipient separating axisymmetric flow. *Trans ASME* I: *J. Fluids Engng* **117**, 433–438.

Singh, R.K. & Azad, R. S. 1995*b* Asymptotic velocity defect profile in an incipient separating axisymmetric flow. *AIAA J.* **33**, 94–101.

Smits, A. J., Eaton, J. & Bradshaw, P. 1979 The response of a turbulent boundary layer to lateral divergence. *J. Fluid Mech.* **94**, 243–268.

Smits, A. J. & Wood, D. H. 1985 The response of turbulent boundary layer to sudden perturbations. *Ann. Rev. Fluid Mech.*, **17**, 321–358.

So, R. M. C. & Mellor, G. L. 1973 Experiment on convex curvature effects in turbulent boundary layers. *J. Fluid Mech.* **60**, 43–62.

Spalart, P. 1988 Direct simulation of a turbulent boundary layer up to $Re_\theta = 1410$. *J. Fluid Mech.* **187**, 61–98.

Spalart, P. & Watmuff, J. 1993 Experimental and numerical study of a turbulent boundary layer with pressure gradients. *J. Fluid Mech.* **249**, 337–371.

Tennekes, H. & Lumley, J. L. 1972 *A First Course in Turbulence*. MIT Press.

Thomas, P. D. & Middlecoff, J. F. 1980 Direct control of the grid point distribution in meshes generated by elliptic equations. *AIAA J.* **18** 652–656.

Townsend, A. A. 1976 *The Structure of Turbulent Shear Flow*, 2nd Edn. Cambridge University Press.

Tsuji, Y. & Morikawa, Y. 1976 Turbulent boundary layers with pressure gradient alternating in sign. *Aero. Q.* **27**, 15–28.

Vreman, B., Geurts, B. & Kuerten, H. 1994 On the formulation of the dynamic mixed subgrid-scale model. *Phys. Fluids* **6**, 4057–4059.

Webster, D., Degraaff, D. & Eaton, J. K. 1996 Turbulence characteristics of a boundary layer over a two-dimensional bump. *J. Fluid Mech.* **320**, 53–69.

Willmarth, W. W. 1975 Pressure fluctuations beneath turbulent boundary layers. *Ann. Rev. Fluid Mech.* **7**, 13-38.

Wu, X. & Squires, K. D. 1995 Three-dimensional boundary layers over an infinite swept bump and free wing. *Trans. ASME* I: *J. Fluids Engng.* **117**, 605–611.

Wu, X. & Squires, K. D. 1997 Large eddy simulation of an equilibrium three-dimensional turbulent boundary layer. *AIAA J.* **35**, 67–74.

Yang, K. S. & Ferziger, J. H. 1993 Large eddy simulation of turbulent obstacle flow using a dynamic subgrid-scale model. *AIAA J.* **31**, 1406–1413.

Zang, Y. Street, R. & Koseff, J. R. 1993 A dynamic mixed subgrid-scale model and its application to turbulent recirculating flows. *Phys. Fluids* A **5**, 3186–3196.